HEATS Workshop 2026

HEATS Workshop 2026
held at CNR-ISTP Bari on January 15-16, 2026

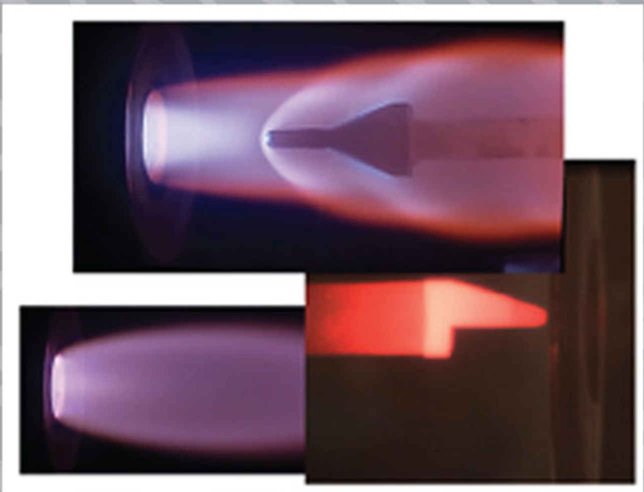

Edited by
Francesco Bonelli, Oreste Pezzi, Anselmo Cecere,
Davide Ninni and Gianpiero Colonna

MRF

HEATS Workshop 2026

HEATS Workshop 2026
held at CNR-ISTP Bari on January 15-16, 2026

Editors

Francesco Bonelli[1], Oreste Pezzi[2],
Anselmo Cecere[3], Davide Ninni[1] and Gianpiero Colonna[3]

[1]Department of Mechanics, Mathematics and Management (DMMM), Politecnico di Bari, Bari, Italy

[2]Institute for Plasma Science and Technology (ISTP), National Research Council of Italy (CNR), Bari, Italy

[3]Department of Industrial Engineering, University of Naples Federico II, Naples, Italy

Peer review statement

All papers published in this volume of "Materials Research Proceedings" have been peer reviewed. The process of peer review was initiated and overseen by the above proceedings editors. All reviews were conducted by expert referees in accordance to Materials Research Forum LLC high standards.

Published under License by **Materials Research Forum LLC**
Millersville, PA 17551, USA

Published as part of the proceedings series
Materials Research Proceedings
Volume 70 (2026)

ISSN 2474-3941 (Print)
ISSN 2474-395X (Online)

ISBN 978-1-64490-428-2 (Print)
ISBN 978-1-64490-429-9 (eBook)

Distributed worldwide by

Materials Research Forum LLC
105 Springdale Lane
Millersville, PA 17551
USA
https://mrforum.com

Manufactured in the United States of America
10 9 8 7 6 5 4 3 2 1

Table of Contents

Preface

This volume collects selected contributions presented at the final workshop of the PRIN 2022 PNRR project **HEATS – Hypersonic Entry flow simulator for Access To Space**, held at CNR ISTP Bari on January 15–16, 2026.

The HEATS project was devoted to the development of advanced computational tools for the simulation of atmospheric super-orbital and lunar re-entry flows in the ionization regime. The project addressed key challenges in hypersonic aerothermodynamics, including high-temperature gas effects, chemical non-equilibrium, dissociation and ionization processes, plasma formation, radio-wave absorption, and the interaction between high-enthalpy flows and Thermal Protection System materials.

The workshop provided an opportunity to present and discuss the main scientific outcomes of the project, bringing the three HEATS research groups — Politecnico di Bari, CNR ISTP Bari, and the University of Naples "Federico II" — together with researchers from the University of Bologna, Politecnico di Torino, CNR ISSMC Faenza, the Italian Aerospace Research Centre (CIRA), the Italian Space Agency (ASI) and the European Space Agency (ESA) all contributing to a fruitful scientific exchange on modelling, simulation, materials, and experiments for hypersonic re-entry applications.

All papers included in this volume underwent a review process before publication. The editors gratefully acknowledge the authors, reviewers, workshop participants, and project partners for their valuable contributions and support.

Further information on the workshop is available at:
https://heats-prin2022pnrr.poliba.it/workshop.php

The HEATS projects was funded by the European Union – Next Generation EU under the Italian National Recovery and Resilience Plan, PNRR, Mission 4 Component 2 Investment 1.1, PRIN 2022 PNRR programme, CUP Master - D53D23018520001, CUP Politecnico di Bari - D53D23018520001, CUP CNR - B53D23027270001, CUP Università degli Studi di Napoli Federico II - E53D23017480001, project **"Hypersonic Entry flow simulator for Access To Space – HEATS"**.

Organizing Committee

Francesco Bonelli (Chair/PI HEATS project - DMMM Politecnico di Bari)

Anselmo Cecere (Università degli Studi di Napoli Federico II)

Oreste Pezzi (CNR ISTP sezione di Bari)

Gianpiero Colonna (CNR ISTP sezione di Bari)

Davide Ninni (DMMM Politecnico di Bari)

Materials Research Proceedings 70 (2026) 1-7 https://doi.org/10.21741/9781644904299-1

Numerical–Experimental Study of Satellite Demise in an Arcjet Wind Tunnel

Sergio CASSESE[1,a *], Stefano MUNGIGUERRA[1,b], Gennaro CORBI[1,c], Anselmo CECERE[1,d] and Raffaele SAVINO[1,e]

[1]Department of Industrial Engineering, University of Naples “Federico II”, Naples, Italy

[a]sergio.cassese@unina.it, [b]stefano.mungiguerra@unina.it, [c]ge.corbi@studenti.unina.it, [d]anselmo.cecere@unina.it, [e]rasavino@unina.it

Keywords: Plasma Wind Tunnel, Hypersonic Flows, Computational Fluid Dynamics, Thermo-Chemical Non-Equilibrium, Debris Risk Assessment, Demise

Abstract. The increasing population of orbital debris poses a growing risk to space operations, making satellite demise evaluation during atmospheric re-entry critical. This study investigates CubeSats (16U and 3U) through an integrated numerical–experimental approach. Trajectory simulations identify critical heat fluxes and altitudes for component destruction, while SPES plasma wind tunnel tests reproduce representative hypersonic conditions. CFD simulations with thermochemical non-equilibrium and thermal simulations of the specimens predict thermal loads in good agreement with experiments, indicating slightly catalytic steel behavior. The results provide validated data for satellite survivability assessment and support laboratory-scale reproduction of realistic re-entry conditions for debris mitigation.

Introduction

Orbital debris refers to any human-made object orbiting Earth that no longer serves a functional purpose, particularly in low Earth orbit (LEO). While recent satellite proliferation is dominated by CubeSats and large constellations, a significant population of small, uncatalogued debris remains a major mission-ending risk [1]. Beyond collision avoidance, understanding satellite demise during atmospheric re-entry is essential for debris mitigation, requiring accurate characterization of materials and thermofluid-dynamic conditions.

This work investigates representative materials to enable future studies on standard CubeSat geometries. In this framework, 3U and 16U configurations are considered as reference cases defining the operational range of re-entry conditions for CubeSat platforms. The study combines trajectory simulations, debris risk assessment, plasma wind tunnel testing and CFD modeling to reproduce and analyze re-entry conditions and material response.

Entry Trajectory Simulations

Re-entry trajectories of standard 16U and 3U CubeSat classes were simulated using a high-fidelity MATLAB model assuming three degrees of freedom, a US76 atmospheric model, and a spherical Earth.

In this work, a fixed and stable attitude is assumed, and equivalent radii for the two configurations are defined to estimate aerodynamic heating, based on a reference area corresponding to the assumed spacecraft orientation. For the heat flux evaluation within the CubeSat re-entry envelope, a one-dimensional correlation based on Zoby’s formula is adopted, which requires the definition of a representative characteristic length (i.e., the equivalent radius).

For the 16U configuration, a limiting case is considered by assuming fully deployed solar panels and the largest exposed area during re-entry (($0.6\ m^2$), where the equivalent radius is obtained using an equivalent spherical surface area. This configuration characterized by a minimum ballistic coefficient, maximizes aerodynamic drag and minimizes the maximum peak heat flux.

For the 3U CubeSat, the opposite limit scenario is defined by assuming malfunctioning or non-deployed solar panels. In this case, the smallest reference area is adopted (0.01 m²), resulting in the highest ballistic coefficient and, consequently, more severe re-entry heating conditions. The equivalent radius is defined as that of a disk with an area corresponding to the satellite face. These assumptions are explicitly intended as bounding cases to envelop the range of possible configurations during the high-dynamic-pressure phase. The geometry and characteristic dimensions, expressed in mm, of the adopted configurations are shown in Fig. 1.

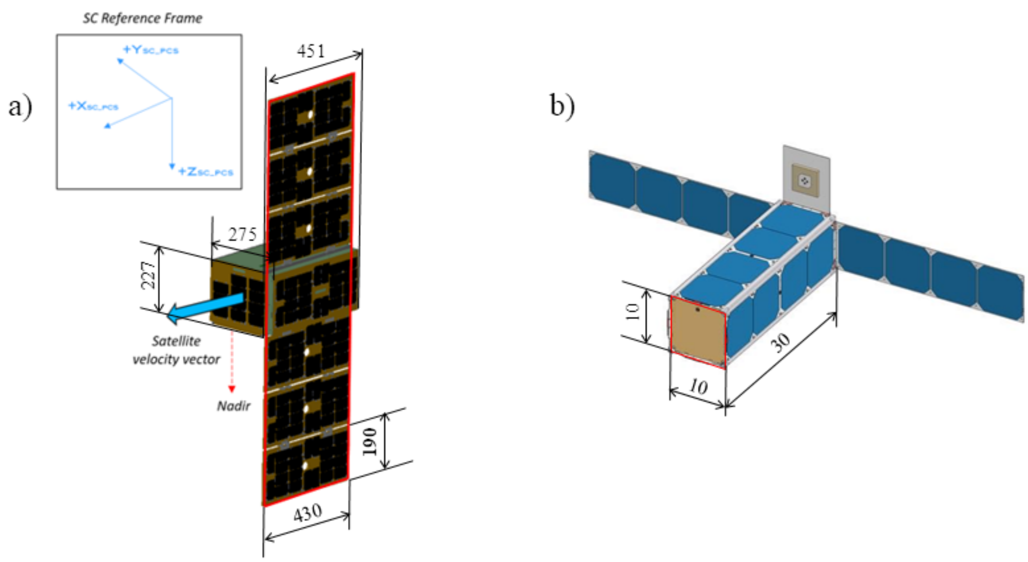

Figure 1: Geometry and characteristic dimensions of standard (a) 16U and (b) 3U CubeSat configurations considered in this study.

The modelling of the drag coefficient is based on an altitude-dependent formulation to account for variations in the flow regime along the trajectory. In particular, the variation is defined through the relationship between drag coefficient and Knudsen number, as derived from literature data [2]. A piecewise-constant approximation of the drag coefficient as a function of altitude is adopted, with the corresponding values reported in Eq. 1:

$$CD(H) = \begin{Bmatrix} 2.5 & H \leq 200\ km \\ 2.0 & 200\ km < H \leq 150\ km \\ 1.5 & 150\ km < H \leq 100\ km \\ 1.0 & H < 100\ km \end{Bmatrix} \quad (1)$$

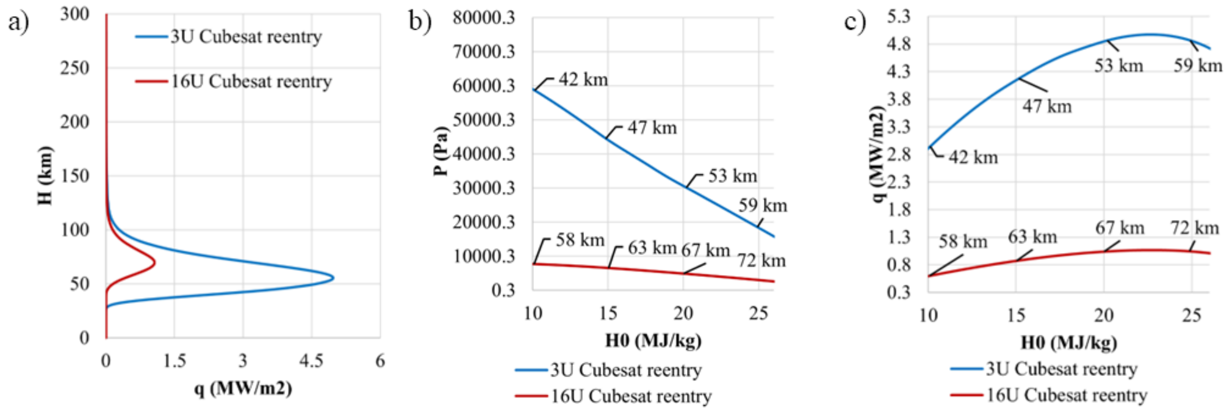

Figure 2: Variation of heat flux with altitude (a); stagnation-point heat flux (b) and stagnation pressure (c) as functions of total enthalpy.

Within each altitude range, the drag coefficient is assumed constant, while variations between layers reflect transitions between different flow regimes. Fig. 2 presents a comparison of the key parameters for both CubeSats.

Debris Risk Assessment

Compliance with orbital debris mitigation requirements was evaluated using NASA's Debris Assessment Software (DAS) [3].

Satellite components were modeled as lumped thermal masses, with demise occurring when absorbed heat exceeded the heat of ablation. DAS analysis conducted between 60 and 80 km altitude predicts complete destruction of all critical components between 75 and 78 km, consistent with the high thermal loads identified in the trajectory simulations.

Numerical Simulation of Debris Flight Conditions in a Plasma Wind Tunnel

Experimental investigations were conducted at the Small Planetary Entry Simulator (SPES) plasma wind tunnel at the University of Naples Federico II, schematically shown in Fig. 3. The facility operates up to 80 kW, with total enthalpy ranging from 3 to 30 MJ/kg and stagnation pressures between 500 and 10,000 Pa, enabling hypersonic flow reproduction representative of re-entry conditions [4, 5].

Cylindrical steel specimens (2 cm diameter, 2 cm downstream of the nozzle) was employed for the preliminary SPES tests to match the CubeSat re-entry envelope. The steel specimen was selected to verify and validate the experimental setup, as it is representative of high-density, high-thermal-inertia structural commonly found in spacecraft, such as fasteners, bolts, threaded inserts, and mounting hardware for electronic boards, which constitute some of the most thermally resistant elements in spacecraft architectures, relevant to demise modelling. The surface temperature of the sample was continuously monitored using a digital two-colour pyrometer (IGAR6, Impac Electronic GmbH, Germany), with a stated accuracy of ±1%, operating in the 1.5–1.6 µm and 2.0–2.5 µm spectral bands and covering a temperature range of 250–2000 °C. The instrument was focused on the stagnation point of the specimen in two-colour mode, where temperature evaluation is based on the radiance ratio, thereby reducing sensitivity to absolute emissivity under the assumption of grey-body behaviour (constant emissivity ratio over the two wavelengths).

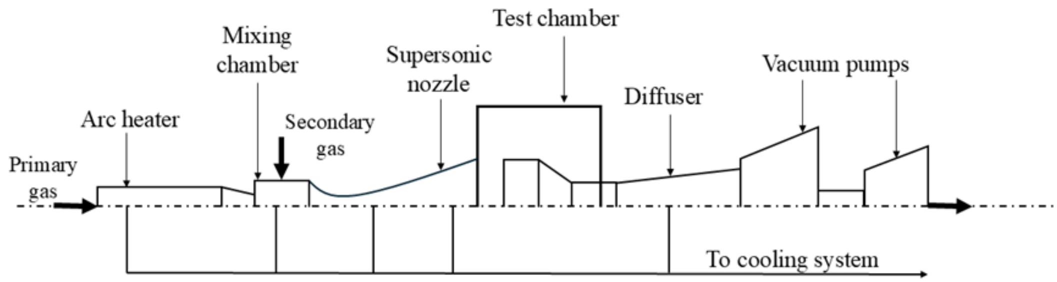

Figure 3: Simplified scheme of the Small Planetary Entry Simulator (SPES), showing main components and flow path.

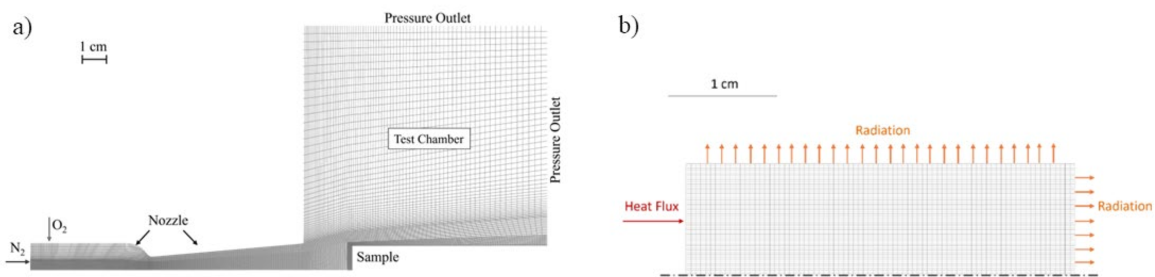

Figure 4: Computational domains for (a) flow simulations and (b) thermal analysis.

Computational Fluid Dynamics (CFD) simulations solved the Reynolds-Averaged Navier-Stokes (RANS) equations with the k-ε turbulence model and thermochemical non-equilibrium using a two-temperature approach with 5 and 11-species air models, adopting the corresponding chemical kinetics and transport property formulations from the literature [6, 7].

Simulations were performed with or without the specimen, accounting for wall catalysis through the implementation of both non-catalytic (NC) and fully catalytic (FC) boundary conditions. The non-catalytic condition is imposed by enforcing zero diffusive flux for each species normal to the surface, while the fully catalytic condition is implemented by specifying complete surface recombination, with sticking coefficients set to unity (γ_N = 1, γ_O = 1). The computational domains for flow and thermal analysis are shown in Fig. 4, A structured mesh was employed to discretize the computational domain, with particular refinement in the near-wall region. The grid was designed to capture boundary layer phenomena while maintaining reasonable computational cost, with finer cells near the wall and coarser resolution in the free stream. The near-wall resolution ensures a dimensionless wall distance $y^+ < 5$ (typically in the range 0.1–2), allowing accurate resolution of the viscous sublayer and reliable heat flux predictions. Walls are treated as fixed boundaries with prescribed temperature of 300 K, whereas radiative heat transfer is neglected, as convective heating is dominant for the considered case.

The test conditions are listed in Table 1 including current, mass flow rate, and specific enthalpy, while the stagnation pressure has been obtained from CFD simulations.

Heat transfer in the 2 cm diameter steel cylinder was modeled within the solid domain to assess its thermal response. In the CFD simulations of the hypersonic plasma flow, the specimen wall temperature was set to 300 K, and the convective heat flux at the surface was extracted.

Table 1: Test conditions.

Parameter	Value
Arc Current	350 A
N_2 mass flow rate	0.4 g/s
O_2 mass flow rate	0.1 g/s
Specific enthalpy (nozzle exit)	13.3 MJ/kg
Stagnation pressure	~ 3000Pa

This heat flux was then used as input for the thermal analysis, which accounts for the transient temperature evolution of the material and radiative heat losses, resulting in a one-way coupling between the flow and solid domains. On the front surface exposed to the plasma, both convective and radiative heat fluxes are considered as shown in Eq. 2:

$$\dot{q} = \dot{q_0}\left(1 - \frac{c_p T_w}{H_0}\right) - \sigma\varepsilon T_w^4 \quad (2)$$

where $\dot{q_0}$ represents the initial heat flux value obtained from plasma wind tunnel simulations, c_p is the specific heat, H_0 is the specific total enthalpy at the nozzle exit, T_w is the average temperature computed at each iteration for the front and lateral walls of the sample, σ is the Stefan--Boltzmann constant ε is the material emissivity. Two surface emissivity values were assumed (0.1 and 0.4), corresponding to polished and oxidized steel surfaces, respectively. Radiation on the back and lateral surface of the sample were considered, while convective heating is negligible due to the low chamber pressure (~ 2 mbar), making radiation the dominant mechanism. Radiative heating from the plasma is neglected, consistent with preliminary analyses of small specimens under low-density flow.

Results and discussion

Steel specimens were exposed to the plasma flow for approximately 50 s, after which melting and material release were observed. Fig. 5 illustrates the specimen evolution during the test. The heat flux incident on the steel specimen (2 cm diameter cylinder) was estimated through an iterative procedure based on surface temperatures measured with a two-color pyrometer. Initial trial heat flux value corresponding to the non-catalytic case was applied in a thermal model including convective and radiative heat transfer, and the resulting surface temperatures were compared with the experimental measurements. This process was repeated until the predicted temperatures were in reasonable agreement with the observations. Surface temperatures measured by a two-color pyrometer (Fig. 6) agree with numerical predictions for a 1.7 MW/m² heat flux.

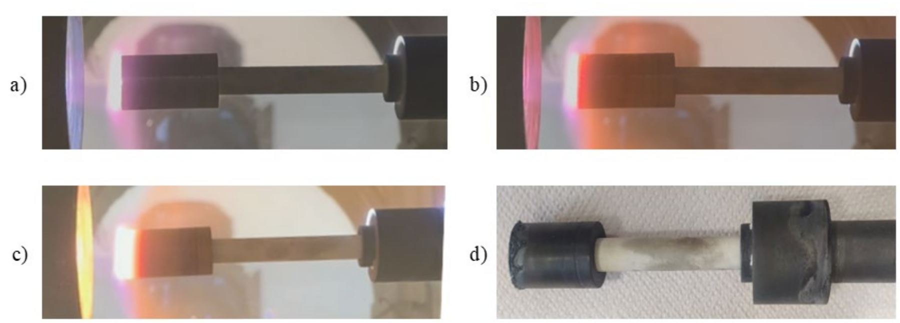

Figure 5: Evolution of the specimen at different stages of the test: (a) 0 s, (b) 30 s, (c) 45s, and (d) specimen condition at the end of the test.

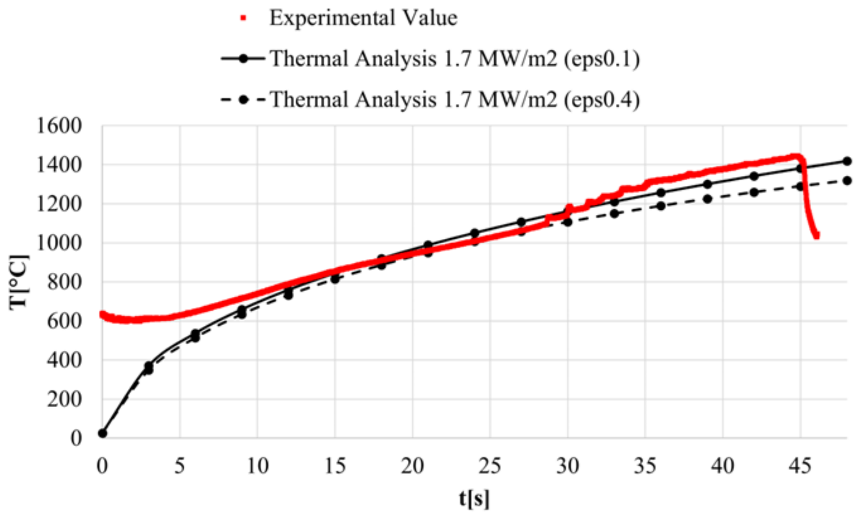

Figure 6: Comparison between experimental and numerical temperature histories for the steel Specimen.

CFD simulations for non-catalytic and fully catalytic wall conditions gave fluxes of 1.2 MW/m² and 2.8 MW/m², respectively, suggesting that the steel shows slight catalytic behavior in air.

Conclusions

An integrated numerical and experimental framework was developed to investigate the demise of small satellite components during atmospheric re-entry. Trajectory simulations and DAS analysis consistently identified critical altitudes and thermal loads leading to component destruction. Plasma wind tunnel experiments successfully reproduced hypersonic re-entry conditions, while CFD simulations accurately predicted flow fields and thermal response.

The agreement between numerical and experimental results supports the validity of the proposed approach for design-for-demise evaluations of CubeSats. Future work will focus on tests with ablative materials and scaled satellite configurations (1:5 of a 3U CubeSat), for which polylactic acid (PLA) was selected to investigate the thermal response of ablative materials and polymers such matrices, and potting agents commonly found in satellite components. Selected for its manufacturability and repeatability, PLA was used as a proxy to characterize the generic fragmentation behavior of non-metallic materials, providing vital support for the validation of numerical modelling. A thorough understanding of these phenomena can improve the simulation of atmospheric break-up and fragmentation sequences of equipment, systems and spacecraft [8].

Acknowledgments

This study was carried out within the Space It Up project funded by Italian Space Agency, ASI, and the Ministry of University and Research, MUR, under contract n. 2024-5-E.0-CUP n.I53D24000060005.

References

[1] C. Ostrom, Introduction to the Orbital Debris Environment and Mitigation Requirements, 39th SmallSat Conference, Salt Lake City, UT, 2025

[2] C. R. Wassgren, J. A. Cordova, R. Zenit, A. Karion Dilute granular flow around an immersed cylinder, Physics of Fluids, November 2003. https://doi.org/10.1063/1.1608937

[3] J. -C. Liou, Debris Assessment Software User's Guide, Orbital Debris Programme Office, Houston (United States), May 2020

[4] S. Mungiguerra, G.D. Di Martino, A. Cecere, R. Savino, L. Silvestroni, A. Vinci, L. Zoli, D. Sciti, Arc-jet wind tunnel characterization of ultra-high-temperature ceramic matrix composites, Corrosion Science, April 2019. https://doi.org/10.1016/j.corsci.2018.12.039

[5] R. Savino, L. Criscuolo, G. D. Di Martino, S. Mungiguerra, Aero-thermo-chemical characterization of ultra-high-temperature ceramics for aerospace applications, J. of the European Ceramic Society, July 2018. https://doi.org/10.1016/j.jeurceramsoc.2017.12.043

[6] C. Park, Review of chemical-kinetic problems of future NASA mission, I: earth entries, J. Thermophys. Heat Transf., Vol. 7, No. 3, pp. 385-393, 1993. https://doi.org/10.2514/3.431

[7] M. G. Dunn, S. Kang, Theoretical and experimental studies of reentry plasmas, NASA Contractor Report 2232, 1973.

[8] European Space Agency, DIVE - Guidelines for Analysing and Testing the Demise of Man Made Space Objects During Re-entry," ESA-TECSYE-TN-018311.

Materials Research Proceedings 70 (2026) 8-11 https://doi.org/10.21741/9781644904299-2

Heat Transfer Analysis of Ultra-High-Temperature Ceramics in Plasma Wind Tunnel Experiments

Anselmo CECERE[1,a*], Dylan DE PRISCO[1,b], Gennaro CORBI[1,c], Raffaele COSTANZO[1,d*], Sergio CASSESE[1,e], Stefano MUNGIGUERRA[1,f] and Raffaele SAVINO[1,g]

[1]Department of Industrial Engineering, University of Naples "Federico II", Naples, Italy

[a]anselmo.cecere@unina.it, [b]dylan.deprisco@unina.it, [c]ge.corbi@studenti.unina.it, [d]raffaele.costanzo@unina.it, [e]sergio.cassese@unina.it, [f]stefano.mungiguerra@unina.it, [g]rasavino@unina.it

Keywords: Hypersonic Flows, UHTC Materials, Thermo-Chemical Nonequilibrium, Atmospheric ReEntry

Abstract The transient thermal response of ZrB_2-SiC is investigated in Plasma Wind Tunnel tests using the Small Planetary Entry Simulator, an arc jet facility capable of simulating the harsh conditions of atmospheric reentry with total specific enthalpies up to 20 MJ/kg. Numerical analyses of the high enthalpy flow are carried out considering thermal and chemical non-equilibrium conditions and catalytic surface recombination coefficients of the ZrB_2-SiC sample. Results showed thermal and chemical non equilibrium flow conditions for the generated plasma and a weakly catalytic behavior for this type of materials.

Introduction

During the reentry phase of a space system, the huge amount of kinetic energy reached by a vehicle flying at speeds ranging from 7.8 km/s for low Earth orbit to around 12.5 km/s for the Stardust probe, is partially converted into internal energy of the gas, activating the vibrational degrees of freedom, their dissociation and even ionization. The high-enthalpy flows and the heat generated by the gas pose several challenges in the material selection to withstand re-entry conditions without failure [1]. Physical model for a correct description of the convective heat exchange and out-performing high temperature materials are needed to ensure safe atmospheric entries. Ultra High Temperature Ceramics (UHTCs) based on zirconium diboride (ZrB_2) and silcon carbide (SiC) are well-known materials studied for uses as sharp leading-edge components on hypersonic flight vehicles [2]. They have extremely high melting points and exhibit good dimensional stability with respect to other refractory materials which rapidly fail by melting, spalling, pyrolyzing, or ablating. In this work the performances of a ZrB_2/SiC composite have been investigated in a series of plasma wind tunnel experiments in a stagnation point configuration using the Small Plantery Entry Simulator. The convective heat flux has been measured through a coaxial thermocouple embedded in a fully catalytic material having the same geometry as the sample considered, while the thermal response of the UHTC sample is simulated considering several recombination coefficients.

The Small Planetary Entry Simulator

The SPES facility shown in Figure 1a), is a blowdown plasma wind tunnel available at the Department of Industrial Engineering of the University of Naples Federico II, capable of simulating high enthalpy flow conditions that typically a space capsule experiences during a reentry into the Earth's atmosphere. The facility has been already used for ceramics [3-6] and for simulating entry conditions into Titan's atmosphere [7]. Figure 1b) shows some typical experiments carried out with this facility.

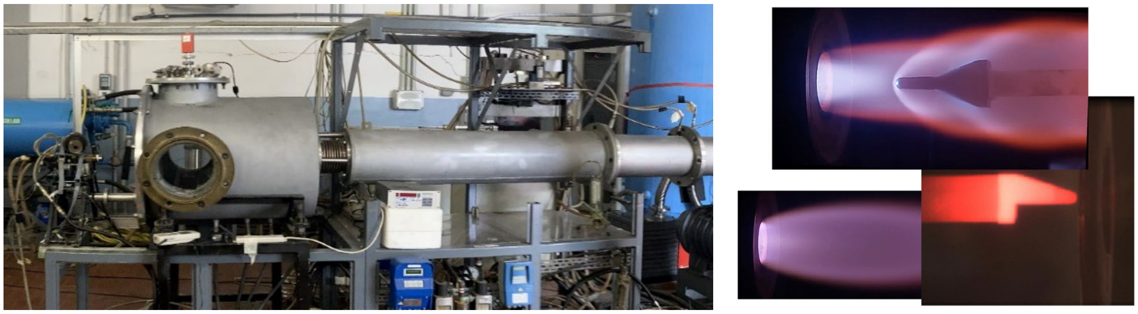

a) b)

Figure 1: a) The Small Planetary Entry Simulator (SPES), b) typical experiment carried out with the SPES facility.

Typical experiments involve the generation of a supersonic high enthalpy flow at relatively low pressure with the aid of an arc heater. An inert or poorly chemically reactive gas (helium, argon, nitrogen and their compounds) is injected into a plasma torch (Sulzer-Metco type 9-M). Gas particles are energized crossing the arc heater and then mixed with a most reactive secondary gas (oxygen, carbon dioxide, methane or others) in a mixing chamber. Supersonic reactive mixtures (Mach 3-5) can be obtained in the test chamber at relatively low pressure using several interchangeable converging-diverging nozzles (area ratio 4, 20, 56, 100). With a mass flow rate in the order of 1 g/s and an expansion ratio of 4, the Mach number and total specific enthalpy at the nozzle exit can reach values of approximately 3 and 15 MJ/kg respectively, with a pressure chamber of 2 mbar. Optical access allows the non-intrusive inspection of both free stream flow conditions, and the thermal behavior of some relatively small samples exposed to the high enthalpy flow. In Table 1 are summarized the tests condition obtained during the experiments.

Table 1: Test parameters for the plasma wind tunnel experimental campaign.

Mass Flow Rate - N_2	**Total Mass Flow Rate**	**O_2 Concentration**	**Specific total enthalpy (torch exit)**	**Specific total enthalpy (nozzle exit)**	**Torch Power**
[g/s]	[g/s]	[%]	[MJ/kg]	[MJ/kg]	[kW]
0.8	1	20	35.1	16.8	30,8

Experimental and numerical results

Three experiments were carried out in the SPES facilities using a ZrB_2-SiC sample in stagnation point configuration. During the experiments the transient temperature of the top surface was monitored with the aid of a pyrometer in a single wavelength configuration, see figure 2b). The acquired signal was converted in temperature considering the spectral emissivity of the sample material in the wavelength of the pyrometer (1.5µm). Numerical simulations were carried out considering the Park 93 two-temperature model, Figure 2a).

Numerical results show thermal and chemical non equilibrium conditions at the nozzle exit and a convective heat flux in order of 5-6 MW/m^2. The computed heat flux under fully catalytic condition was compared with the experimental one measured with the aid of the heat flux probe obtaining a good agreement between the experiment and the numerical code.

Materials Research Proceedings 70 (2026) 8-11 https://doi.org/10.21741/9781644904299-2

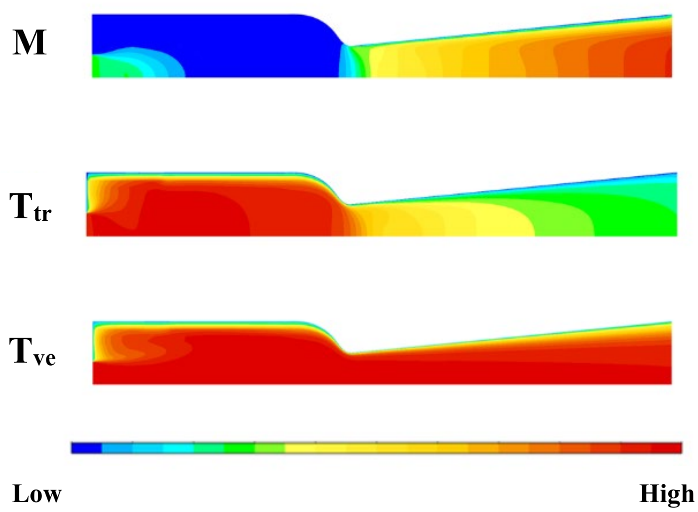

a)

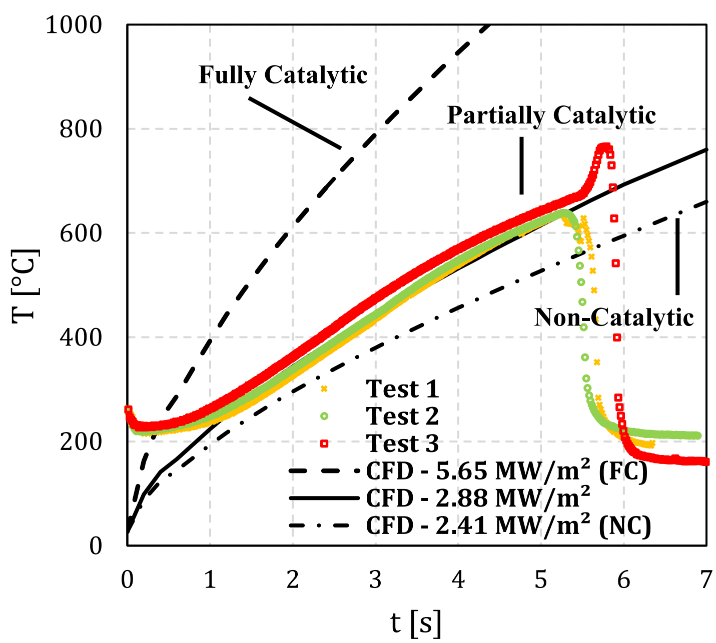

b)

Figure 2: a) Mach number (M), translational-rotational temperature (T_{tr}) and vibrational-electronic temperature (T_{ve}) occurring in the nozzle of the plasma wind tunnel showing non equilibrium conditions at the nozzle exit, b) comparison between experimental and numerical results of the transient temperature rising for the ZrB_2-SiC sample.

The transient thermal response of the ZrB_2-SiC sample was simulated considering fully catalytic, non-catalytic and partially catalytic recombination coefficients for nitrogen and oxygen. According with literature data [8], a good comparison between experimental and numerical results was obtained only if a partially catalytic condition is considered.

Conclusions
This study successfully simulated the thermal behavior of a ZrB_2-SiC ceramic in plasma wind tunnel experiments. Numerical analysis showed thermal and chemical non-equilibrium flow conditions, and a weakly catalytic effect for this type of materials was taken into account to better fit data.

Acknowledgments
The work is funded by the European Union – Next Generation EU – Piano Nazionale Resistenza e Resilienza (PNRR), Missione 4 Componente C2 Investimento 1.1 – Decreto Direttoriale n. 1409 del 14/09/2022, Bando PRIN 2022 PNRR, CUP Master - D53D23018520001, CUP E53D23017480001, Hypersonic Entry flow simulator for Access To Space – HEATS

References
[1] J. D. Schmisseur, "Hypersonics into the 21st century: A perspective on AFOSR-sponsored research in aerothermodynamics", Progress in Aerospace Sciences, Volume 72, January 2015. https://doi.org/10.1016/j.paerosci.2014.09.009

[2] A. Cecere, R. Savino, C. Allouis, F. Monteverde, Heat transfer in ultra-high temperature advanced ceramics under high enthalpy arc-jet conditions, International Journal of Heat and Mass Transfer, Volume 91, 2015, Pages. 747-755. https://doi.org/10.1016/j.ijheatmasstransfer.2015.08.029

[3] S. Mungiguerra, G.D. Di Martino, A. Cecere, R. Savino, L. Silvestroni, A. Vinci, L. Zoli, D. Sciti, "Arc-jet wind tunnel characterization of ultra-high-temperature ceramic matrix composites", Corrosion Science, Volume 149, 1 April 2019, Pages 18-28.

[4] D. Sciti, et al., "Elevated temperature performance: Arc-jet testing of carbon fiber reinforced ZrB2 bars up to 2200 °C for strength retention assessment", Journal of Advanced Ceramics, vol. 14, 2025. https://doi.org/10.26599/JAC.2024.9221022

[5] L. Silvestroni, R. Savino, A. Cecere, S. Mungiguerra, "Failure tolerant functionally graded fiber-reinforced UHTCs exposed to hypersonic flows", Composites Part A: Applied Science and Manufacturing, vol. 185, 2024. https://doi.org/10.1016/j.compositesa.2024.108293

[6] R. Savino, M. De Stefano Fumo, D. Paterna, A. Di Maso, F. Monteverde, "Arc-jet testing of ultra-high-temperature-ceramics", Aerospace Science and Technology, Volume 14, Issue 3, April-May 2010, Pages 178-187. https://doi.org/10.1016/j.ast.2009.12.004

[7] V. Carandente, R. Savino, A. Esposito, G. Zuppardi, V. Caso, "Experimental and numerical simulation, by an arc-jet facility, of hypersonic flow in Titan's atmosphere", Experimental Thermal and Fluid Science, Volume 48, July 2013, Pages 97-101. https://doi.org/10.1016/j.expthermflusci.2013.02.012

[8] Marschall J., et al., "Catalytic Atom Recombination on ZrB2-SiC and HfB2-SiC Ultra-high-Temperature Ceramic Composites", J. Spacecraft Rockets, (2004). https://doi.org/10.2514/1.2879

Materials Research Proceedings 70 (2026) 12-15 https://doi.org/10.21741/9781644904299-3

State-to-State and Macroscopic Models for Earth Atmospheric Entry

Gianpiero COLONNA[1,a *], Lucia Daniela PIETANZA[1,b], Davide NINNI[2,c], Giuseppe PASCAZIO[2,d], Francesco BONELLI[2,e], and Annarita LARICCHIUTA[1,f]

[1]CNR-ISTP Bari, Via Amendola 122/D, 70126 Bari Italy

[2]DMMM-Politecnico di Bari, Via Orabona 4, 70126 Bari, Italy

[a]gianpiero.colonna@cnr.it, [b]luciadaniela.pietanza@cnr.it, [c]davide.ninni@poliba.it, [d]giuseppe.pascazio@poliba.it, [e]francesco.bonelli@poliba.it, [f]annarita.laricchiuta@cnr.it

Keywords: Atmospheric Entry, Multitemperature Model, State-To-State Model

Abstract. A multitemperature model for air, including processes induced by free electrons, has been constructed from a detailed state-to-state kinetics. State-specific dissociation and ionization rates for nitrogen have been reported, together with the electron energy relaxation times for the neutral species.

Introduction

A critical point of a space mission is the entry in the planetary atmosphere [1]. The shock wave formed around the vehicle during hypersonic entry dissipates its kinetic energy in thermal and chemical channels, determining the surface heat flux. Modeling this phenomenon is a complex problem, due to the strong coupling between the flow and chemistry and to the presence of non-equilibrium between the translational, internal and chemical degrees of freedom [2]. Depending on the entry velocity, in the shock wave different processes can be activated, namely molecular excitation, dissociation or even ionization. The most accurate model to properly account of non-equilibrium is the state-to-state (StS) approach [3], that is gaining ground in the aerothermodynamic community. The StS model accounts for the structure of molecules by considering each relevant internal level as an independent pseudo-species by adding specific mass continuity equations [4]. As an example, for diatomic molecules, the vibrational levels of the ground electronic state are considered separately, whose number ranges from few tenth to one hundred, and the system of fluid dynamic equations becomes very large, making difficult the solution for 2D/3D geometries. The use of GPUs, speeding up the computation by 2 orders of magnitude for the StS approach [4], allowed to perform such calculations in a reasonable time. The advantage remains also for mT model, speeding up the calculation by a factor 50 and by a factor 20 under perfect gas assumption. The GPU calculation time scales linearly with the number of cells and with the chemical problem dimension. Another way to describe thermal non-equilibrium is the multi-temperature (mT) approach [1,2], where relevant degrees of freedom are described by independent temperatures, thus considerably reducing the number of equations. Conventional mT models [2] uses Arrhenius rates for chemical processes, depending on an effective temperature calculated as the weighted geometrical mean of the temperatures of the degrees of freedom involved in the chemical process. In recent years, it has been demonstrated the higher predictive character of the StS with respect to mT model in reproducing the distance of the shock front from the surface [5]. The main limit of the mT model is to assume a Boltzmann level distribution that cannot account for deviations of high-energy levels, over/under populated due to processes, such as dissociation/recombination, preferentially activated by highly excited molecules. Another relevant aspect of the mT approach is the determination of the amount of internal energy of molecules involved in the reaction, a quantity naturally emerging in the StS model. The chemical kinetics of very high-enthalpy flows faces a further difficulty due to the

Materials Research Proceedings 70 (2026) 11-14 https://doi.org/10.21741/9781644904299-3

presence of free electrons, increasing the complexity of the chemical model that must include a plethora of elementary processes induced by electron impact. Furthermore, free electrons are responsible for the communication blackout, being the quenching of electromagnetic radiation depending on the frequency of elastic collisions [6,7].

In this paper, we briefly describe a general approach to construct a mT model starting from the StS, and we discuss results of its application to air kinetics [5]. This physically based mT model, not avoiding the Boltzmann distribution assumption, should be considered as a first step towards a reduced kinetics [8] that accounts for non-equilibrium vibrational distributions.

StS and mT models

The mT model here described refers to the vibrational kinetics of the ground electronic state of diatomic molecules, while electronic excited states are kept as separate levels. For the sake of simplicity, in the following the N_2 molecule is taken as an example.

Within a StS scheme, it is possible to define two classes of processes induced by collision with a generic species X and involving vibrationally excited species: the first entails internal transitions ($N_2(v)+X \Leftrightarrow N_2(w)+X$) and the second chemical reactions ($N_2(v)+X \Leftrightarrow p$, p stands for all the possible products). The former contributes, in the mT model, to the vibrational energy equation only. The vibrational energy relaxation rates, K_{vx}, due to internal transitions induced by the species X, are calculated assuming the gas temperature T and a vibrational Boltzmann distribution $f_B(T_v,v)$ at a given temperature T_v with the equation

$$K_{vx}(T,T_v)=\sum_{v,w}k_{x,v\to w}(T)(E_w-E_v)\, f_B(T_v,v) \quad (1)$$

where $k_{x,v\to w}(T)$ is the state specific rate and E_v's are the energy levels. The vibrational energy relaxation time $\tau_x(T,T_v)$, for collisions with a generic species X, entering in the Landau-Teller equation, is given as [9]

$$N_x\tau_x(T,T_v)=[E_{vib}(T)-E_{vib}(T_v)]/\, K_{vx}(T,T_v) \quad (2)$$

where N_x is the density of the X species, $E_{vib}(T_v)=\sum_v E_v\, f_B(T_v,v)$.

For chemical reactions, we need to distinguish between direct and reverse processes: the global chemical rate K_{dx} and that of energy loss K_{dvx} are calculated from the state-specific rates $k_{dx,v\to p}$ as

$$K_{dx}(T,T_v)=\sum_v k_{dx,v\to p}(T)\, f_B(T_v,v) \qquad K_{dvx}(T,T_v)=\sum_v k_{dx,v\to p}(T)\, E_v\, f_B(T_v,v) \quad (3)$$

and for reverse rate K_{rx} and vibrational energy gain K_{rvx} as

$$K_{rx}(T)=\sum_v k_{rx,v\to p}(T) \qquad K_{rvx}(T)=\sum_v k_{rx,v\to p}(T)\, E_v \quad (4)$$

where $k_{rx,v\to p}$ is the state specific reverse rate calculated from the direct one through the detailed balance principle [3]. The contribution of chemical processes to the vibrational energy equation is given by $K_{rvx}-K_{dvx}$, no further assumption on the fractional distribution is required contrarily to what done in in traditional mT approaches [2]. The same equations are valid for electrons, providing that the state-specific rates are determined from the electron-impact cross sections $\sigma_{v\to p}$ integrated over a Maxwell distribution $f_m(T_e)$

$$k_{de,v\to p}(T_e)=\int v_{el}(\varepsilon)\sigma_{v\to p}(\varepsilon)f_m(T_e)d\varepsilon \quad (5)$$

where v_{el} is the electron velocity. As an example, Fig. 1 reports the state-specific rates of N_2 electron impact dissociation and ionization. It should be noted that the ionization rate is less sensible to the level energy, with respect to dissociation, because the ionization threshold is much higher that the dissociation limit and therefore the increase of the collision energy due to vibrational excitation is only a small percent of the global energy.

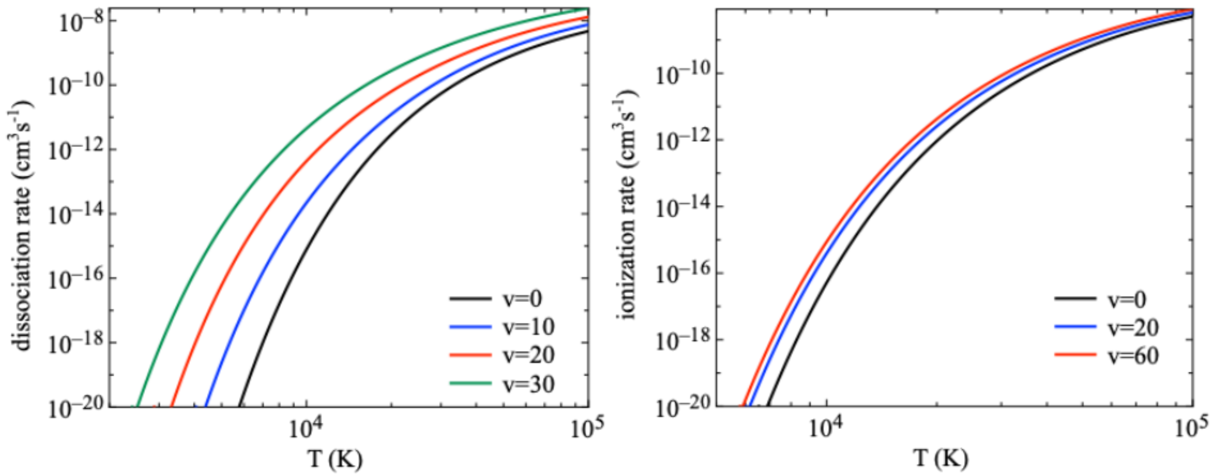

Fig. 1: State-specific rates for N_2 dissociation (left) and ionization (right) by electron impact.

Even if, in the absence of electric field, it is reasonable to assume that the electron energy relaxes rapidly to the gas temperature, for the sake of completeness we have derived the equation for the relaxation of the electron temperature. Two contributions can be envisaged, elastic and inelastic collisions, the latter including both molecular excitation and chemical processes. In inelastic collisions the energy exchanged by electrons is a quantity independent of the electron energy, corresponding to the threshold energy $\varepsilon_v^\star$ of the considered processes, calculated as the difference between transition energy $\varepsilon_0^\star$ from the ground state and E_v. Therefore, the rates of energy exchange are obtained multiplying the chemical/transition rates by $\varepsilon_v^\star$.

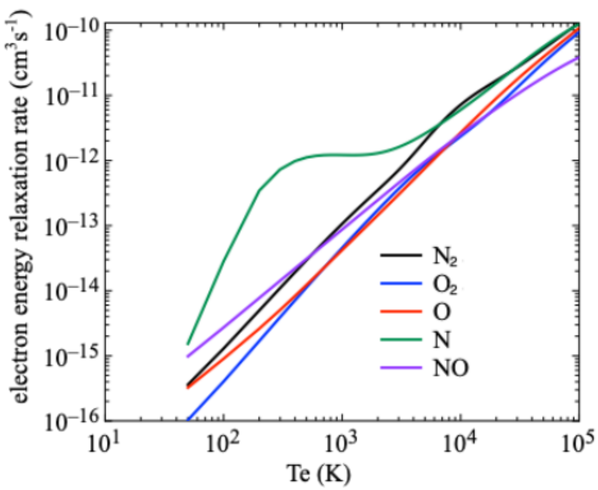

Fig. 2: Electron energy relaxation rate of neutral species in air mixture.

The elastic collisions contribute to the energy equations with a Landau-Teller expression where the relaxation time is related to the sum over species index s of the momentum transfer collision frequency ν_s multiplied by the species density N_s

$$\tau(T_e)=T_e/\sum_s N_s \nu_s(T_e) \qquad \nu_s(T_e)=(2m_e/m_s)\int v_{el}(\varepsilon)\sigma_{mt,s}(\varepsilon)f_m(T_e)d\varepsilon. \tag{4}$$

given the momentum transfer cross section ($\sigma_{mt,s}$), being m_e, m_s electrons and st species mass.

In Fig. 2 the electron energy relaxation rate for the neutral species in the air mixture have been reported as a function of the electron temperature. This quantity is necessary also to calculate the depletion of electromagnetic wave traveling in a plasma, responsible of the communication blackout [7].

Materials Research Proceedings 70 (2026) 11-14 https://doi.org/10.21741/9781644904299-3

Conclusions

The high-fidelity simulation of Earth reentry conditions and the reliable estimation of surface heat flux rely on the accurate modeling of the chemistry activated across the shock. A novel mT model is derived from the StS one developed for air plasmas, that combines the detailed description of elastic, inelastic and reactive processes, in terms of state-specific rate coefficients resolved on the vibrational degree of freedom, with proper relaxation equations for the vibrational energy, ensuring the computational feasibility of the fluid dynamic simulations powered via GPUs.

The computational time of the code [4] scales with the number of the chemical and internal temperature equations, therefore the mT model for ionized air is ten time faster than StS approach. A detailed analysis of the performances of the mT model for hydrogen mixture, both in shock and nozzle conditions, can be found in ref. [8], where it is shown that StS results can be accurately reproduced by the mT, even if some deviations in the molar fraction of minority species are observed in the expansion regime, due to the marked non-equilibrium in the distribution tails. It is worth mentioning that in 2D calculations, the mT and StS results well match.

Acknowledgements

G.C., L.D.P., G.P., F.B., A.L. were funded by the European Union – Next Generation EU – Piano Nazionale Resistenza e Resilienza (PNRR), Missione 4 Componente C2 Investimento 1.1 – Decreto Direttoriale n. 1409 del 14/09/2022, Bando PRIN 2022 PNRR, CUP Master - D53D23018520001, CUP Politecnico di Bari - D53D23018520001, CUP CNR - B53D23027270001, Hypersonic Entry flow simulator for Access To Space – HEATS.

References

[1] J. Anderson, Hypersonic and High-Temperature Gas Dynamics, Mcgraw-Hill Book Company, 1988. https://doi.org/10.2514/5.9781624105142.0000.0000

[2] C. Park. Nonequilibrium Hypersonic Aerothermodynamics. John Wiley & Sons, 1990. https://doi.org 10.1017/S0022112091230657

[3] G. Colonna, M. Capitelli, L. D. Pietanza, Self-consistent kinetics, in: G. Colonna, A. D'Angola (Eds), Plasma Modeling (Second Edition), IOP Publishing, 2022, pp 9.1-9.41 https://doi.org/10.1088/978-0-7503-3559-1ch9

[4] G. Pascazio, D. Ninni, F. Bonelli, G. Colonna, Hypersonic flows with detailed state-to-state kinetics using a GPU cluster, in: G. Colonna, A. D'Angola (Eds), Plasma Modeling (Second Edition), IOP Publishing, 2022, pp 10.1-10.41. https://doi.org/10.1088/978-0-7503-3559-1ch10

[5] G. Colonna, F. Bonelli, G. Pascazio, Impact of fundamental molecular kinetics on macroscopic properties of high-enthalpy flows: The case of hypersonic atmospheric entry. Phys. Rev. Fluids 4 (2019) 033404. https://doi.org/10.1103/PhysRevFluids.4.033404

[6] P. Kozlov, N. Bykova, G. Y. Gerasimov, V. Y. Levashov, M. Kotov, I. Zabelinsky. Radiation properties of air behind strong shock wave. Acta Astronautica 214 (2024) 303–315. https://doi.org/10.1016/j.actaastro.2023.10.033

[7] O. Pezzi, D. Ninni, F. Bonelli, G. Colonna, Radio-wave absorption during capsule re-entry in atmosphere: a numerical study, Materials Research Proceedings MRF LLC, submitted

[8] G Colonna, LD Pietanza, M Capitelli,Recombination-assisted nitrogen dissociation rates under nonequilibrium conditions, J. Thermoph. Heat Transf. 22 (2019) 399-406. https://doi.org/10.2514/1.33505

[9] G. Colonna, L. Walpot, D. Ninni, F. Bonelli, G. Pascazio, L. D. Pietanza, A. Laricchiuta, Multi-temperature model from state-specific data for hydrogen/helium mixture in high-enthalpy flows, Int. J. Heat Mass Transf. 259 (2026) 128376. https://doi.org/10.1016/j.ijheatmasstransfer.2026.128376

Analysis of Thermochemical Non-Equilibrium and Heat Loads in a Mars-like Plasma Flow

Raffaele COSTANZO[1,a], Stefano MUNGIGUERRA[1,b], Gennaro CORBI[1,c], Sergio CASSESE[1,d,*], Anselmo CECERE[1,e], Frederick MONTEVERDE[2,f] and Raffaele SAVINO[1,g]

[1]Department of Industrial Engineering, University of Naples “Federico II”, Naples, Italy

[2]Institute of Science, Technology and Sustainability for Ceramics, National Research Council of Italy, 48018 Faenza, Italy

[a]raffaele.costanzo@unina.it, [b]stefano.mungiguerra@unina.it, [c]ge.corbi@studenti.unina.it, [d]sergio.cassese@unina.it, [e]anselmo.cecere@unina.it, [f]frederic.monteverde@issmc.cnr.it, [g]rasavino@unina.it

Keywords: Hypersonic Flows, Computational Fluid Dynamics, Thermo-Chemical Non-Equilibrium, Martian Atmosphere

Abstract. Atmospheric entry involves hypersonic speeds and extreme thermal loads, inducing complex aero-thermo-chemical non-equilibrium. This study investigates Mars-like plasma flows (CO_2 and N_2) through experimental and numerical methods. Testing at the University of Naples Federico II's SPES arc-jet facility covered enthalpies of 16-20 MJ/kg. Optical Emission Spectroscopy (OES) identified spectra dominated by CN transitions and atomic oxygen. Numerical RANS simulations using a k-ε turbulence model and a 16-species two-temperature (2T) approach showed high correlation with experimental data. Validation via button-shaped specimen thermal history confirmed stagnation point heat fluxes of approximately 2.74 MW/m^2. These results establish a robust methodology for simulating Martian entry and studying material responses like catalyticity and oxidation.

Introduction

Atmospheric re-entry involves hypersonic speeds (≈ 7 km/s) and enthalpies near 30 MJ/kg, triggering vibrational excitation, dissociation, and ionization. These conditions create complex thermochemical non-equilibrium and surface recombination, making ground simulation difficult, particularly for Mars' CO_2-rich atmosphere. Research using shock tubes and arc-jets has emphasized the temperature sensitivity of CO radiation [1], while facilities like HYMETS and ARMSEF have assessed CO_2 entry hazards and gas formation [2]. Advanced tools like the CoRaM-MARS model [3] and physics-based chemistry models [4] improve predictions of non-equilibrium flows and reaction rates. Despite these advantages, gaps remains in modeling convective/radiative heating and surface catalysis, necessitating further validated experimental and computational frameworks [5].

Experimental Facility and Methodology

Experiments were conducted using the Small Planetary Entry Simulator (SPES) [6] at the University of Naples Federico II, a supersonic arc-jet facility. Martian atmospheres were simulated using CO_2/N_2 mixtures, expanded to Mach 3 with enthalpies near 20 MJ/kg. With a power of up to 80 kW, SPES facilitates stagnation pressures between 500 and 10,000 Pa. Diagnostics include Pitot probes and calorimeters for pressure and heat flux, plus infrared cameras and pyrometers for temperature. Optical Emission Spectroscopy (OES) was performed 1 cm downstream of the nozzle exit using an Ocean Optics USB2000 spectrometer to characterize plasma chemical species and non-equilibrium states during free-jet tests. Material tests involved button-shaped specimens

Materials Research Proceedings 70 (2026) 16-19 https://doi.org/10.21741/9781644904299-4

insulated in mullite tubes and exposed to stabilized conditions for 3 seconds. Stagnation temperatures and surface gradients were recorded via pyrometry and infrared cameras to validate Computational Fluid Dynamics (CFD) and thermal models.

Table 1: Test parameters for CO_2-based plasma experimental campaigns.

Test	Mass Flow Rate - N_2	Total Mass Flow Rate	CO_2 Concentration	Specific total enthalpy (torch exit)	Specific total enthalpy (nozzle exit)	Torch Power
	[g/s]	[g/s]	[%]	[MJ/kg]	[MJ/kg]	[kW]
A1	0.8	1.2	33	34.2	16.2	36.3
A2	0.8	1	20	34.2	16.8	36.3
B1	0.4	0.8	50	50.5	18	29.15
B2	0.4	0.6	33	50.5	20.2	29.15

Table 1 summarizes the tests condition. Tests A1 and A2 focus on heat flux evaluation and investigation, tests B1 and B2 instead focus on spectra acquisition and analysis.

Numerical Modeling

Fluid dynamics are simulated via Reynolds-Averaged Navier-Stokes (RANS) equations and the k-ε turbulence model across a domain spanning from the torch exit to the test chamber. Simulations utilize 300 Pa pressure and 400 K non-catalytic wall conditions, employing 1T and 2T [7] thermal models to distinguish T_{tr} and T_{ve}. A 16-species kinetic model, including CN, is used to accurately capture Martian plasma chemistry. Radiative properties are characterized using SPECAIR [8], which generates emission spectra from CFD data (translational-rotational temperature T_{tr}, vibrational-electronic temperature T_{ve}, and mole fractions). These results are convolved with a calibrated slit function to account for instrumental broadening, allowing for direct comparison with experimental OES data to validate the plasma's thermochemical state.

Numerical Results

Experimental data and numerical modeling characterized the Mars-like plasma flow, focusing on the effect of operating conditions on enthalpy, spectral chemical identification, and specimen thermal loads.

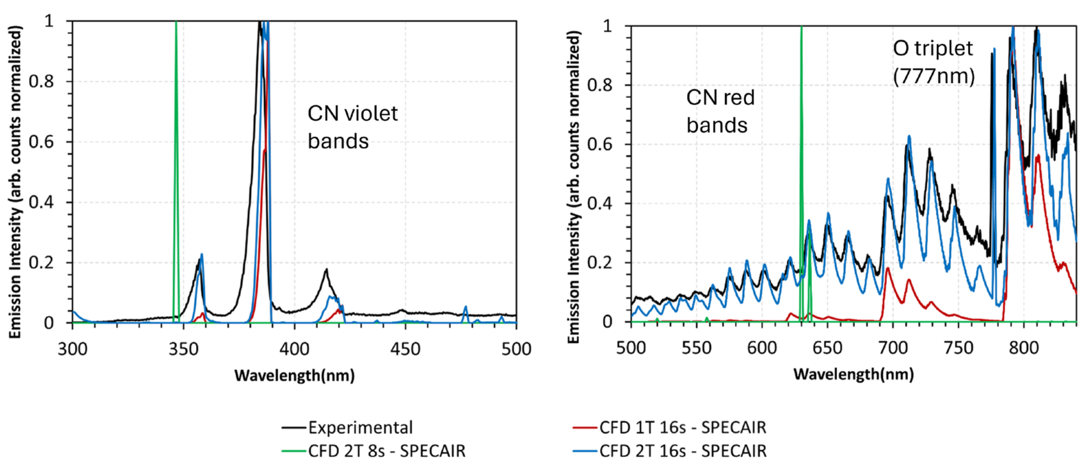

Figure 1: Experimental-Numerical Spectrum Correlation.

Plasma enthalpy has been shown to be highly sensitive to gas composition. By reducing N_2 or CO_2 flow rates, the specific total enthalpy increased at the nozzle exit, with target Martian entry values ranging from 16 to 20 MJ/kg. Optical Emission Spectroscopy (OES) showed spectra dominated by CN violet and red systems, with atomic oxygen (777 nm triplet) also present, matching air plasma signatures. The SPECAIR synthetic spectra in the 500-850 nm band validated the inadequacy of the 1T and 16-species models, while the 2T-CFD model with 16 species provided the best fit, confirming the necessity of accounting for CN and thermochemical non-equilibrium (Figure 1). Significant divergence was observed between vibro-electronic (≈5700 K) and roto-translational (≈1700 K) temperatures.

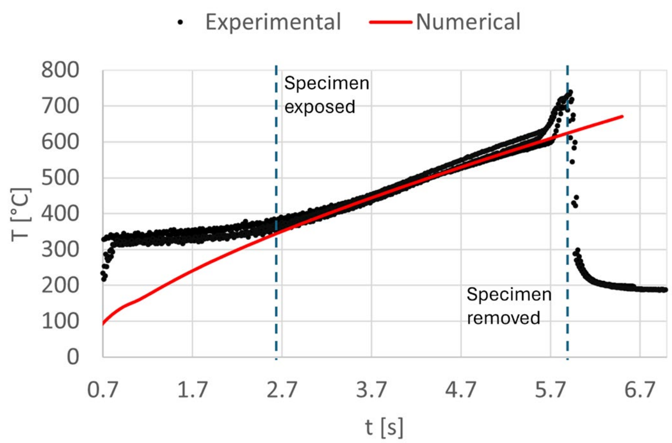

Figure 2: Thermal History Reconstruction.

Heat flux was evaluated using button-shaped specimens exposed for 3 seconds, with surface temperatures monitored via pyrometer. Numerical simulations assuming a non-catalytic wall predicted a stagnation point heat flux of 2.74 MW/m^2. This numerical approach accurately reproduced experimental temperature rises, validating the model for Martian entry thermal environments (Figure 2).

Conclusions

Characterizing atmospheric re-entry is challenging due to extreme velocities and thermochemical non-equilibrium. This study successfully simulated Martian entry using the SPES arc-jet facility, generating stable plasma jets with relevant total enthalpies. Spectroscopy revealed emission dominated by CN transitions and atomic oxygen. Numerical results showed that standard one-temperature models are insufficient; instead, a two-temperature 16-species RANS model including CN provided high correlation with experimental data by capturing nozzle-exit non-equilibrium. The predicted stagnation heat flux of 2.74 MW/m2 was validated by experimental surface temperature reconstructions, confirming the framework's reliability for CO_2-rich atmospheres. Future research at UNINA will focus on testing different materials in extreme plasma environments with varying CO_2 concentrations and conduct long-duration tests on materials to investigate wall catalyticity, oxidation, and evolving spectral emissivity under high-temperature exposure

References

[1] A. M. Brandis et al., «Validation of CO 4th positive radiation for Mars entry», J. Quant. Spectrosc. Radiat. Transf., vol. 121, pp. 91–104, mag. 2013. https://doi.org/10.1016/j.jqsrt.2013.02.009

[2] S. C. Splinter, K. S. Bey, J. G. Gragg, e A. Brewer, «Comparative Measurements of Earth and Martian Entry Environments in the NASA Langley HYMETS Facility», presentato al American Inst. of Aeronautics and Astronautics, United States, gen. 2011. Consultato: 25 settembre 2025. [Online]. Disponibile su: https://ntrs.nasa.gov/citations/20110003632

[3] J. Annaloro e A. Bultel, «Vibrational and electronic collisional-radiative model in CO2-N2-Ar mixtures for Mars entry problems», Phys. Plasmas, vol. 26, fasc. 10, p. 103505, ott. 2019. https://doi.org/10.1063/1.5114792

[4] R. L. Jaffe, D. W. Schwenke, G. M. Chaban, D. K. Prabhu, C. O. Johnston, e M. Panesi, «On the development of a new nonequilibrium chemistry model for Mars entry», in 55th AIAA Aerospace Sciences Meeting, Grapevine, Texas: American Institute of Aeronautics and Astronautics, gen. 2017. doi: 10.2514/6.2017-1372

[5] M. J. Wright, C. Y. Tang, K. T. Edquist, B. R. Hollis, e P. Krasa, «A Review of Aerothermal Modeling for Mars Entry Missions», presentato al American Inst. of Aeronautics and Astronautics, United States, dic. 2009. Consultato: 25 settembre 2025. [Online]. Disponibile su: https://ntrs.nasa.gov/citations/20100021401

[6] S. Mungiguerra, G. D. Di Martino, e G. Zuppardi, «Computational Evaluation of Aero-Thermodynamic Loads and Effect of Catalyticity in an Arc-Jet Wind Tunnel», J. Aerosp. Eng., vol. 33, fasc. 3, p. 04020005, mag. 2020. https://doi.org/10.1061/(ASCE)AS.1943-5525.0001114.

[7] P. A. Gnoffo, R. N. Gupta, e J. L. Shinn, «Conservation equations and physical models for hypersonic air flows in thermal and chemical nonequilibrium». 1 febbraio 1989. Consultato: 12 giugno 2025. [Online]. Disponibile su: https://ntrs.nasa.gov/citations/19890006744

[8] SPECAIR, «SPECAIR v3.0 user manual», SpectralFit, 2024. [Online]. Disponibile su: http://www.specair-radiation.net/manual.php

Materials Research Proceedings 70 (2026) 20-24 https://doi.org/10.21741/9781644904299-5

Three-Dimensional CFD Analysis of Ionization Asymmetries in the RAM-C II Reentry Experiment

Luigi CUTRONE[1,a *], Salvatore ESPOSITO[1,b] and Antonio SCHETTINO[1,c]

[1]Italian Aerospace Research Center (CIRA), Capua, Italy

[a]l.cutrone@cira.it, [b]s.esposito@cira.it, [c]a.schettino@cira.it

Keywords: Aerothermodynamics, Ionization, Computational Fluid Dynamics

Abstract. This work investigates the influence of angle of attack (AoA) on plasma formation during the RAM-C II reentry experiment using a three-dimensional, non-equilibrium CFD framework. Simulations were performed across altitudes of 61–81 km with AoA ranging from -4° to +4° using an 11-species ionizing air model. The numerical results, which successfully capture the data spread observed in flight measurements, reveal strong windward–leeward plasma asymmetries that underscore the critical role of vehicle attitude in predicting hypersonic environments. This sensitivity diminishes at higher altitudes due to reduced chemical activity and increased diffusion.

Introduction

Accurate prediction of plasma formation in hypersonic reentry flows is essential for understanding communication blackout phenomena and vehicle–plasma interactions [1]. At high velocities and altitudes, strong shock waves induce intense heating, leading to dissociation and partial ionization of atmospheric air and the formation of a weakly ionized plasma sheath surrounding the vehicle. Even small electron concentrations significantly affect electromagnetic wave propagation and signal attenuation [2,3].

The RAM-C II flight experiment represents one of the most comprehensive in-flight datasets for electron density measurements during atmospheric entry and has been widely used as a benchmark for validating numerical plasma flow models [4,5]. Most previous numerical studies of RAM-C II have focused on axisymmetric or quasi-two-dimensional configurations [6,7,8,9], which inherently neglect three-dimensional flow effects and asymmetries induced by vehicle attitude.

However, during flight the RAM-C II payload experienced oscillations in angle of attack due to spin and atmospheric disturbances, leading to significant windward–leeward asymmetries in the plasma layer observed by onboard diagnostics. Capturing such three-dimensional effects is essential for accurately reproducing the measured electron density distributions.

In this work, a validated non-equilibrium CFD framework is extended to fully three-dimensional simulations of the RAM-C II vehicle to investigate the influence of angle of attack on plasma generation and spatial electron density distributions across a range of reentry altitudes [10]. The study focuses exclusively on three-dimensional effects, assuming thermochemical modeling parameters previously assessed in two-dimensional simulations [11].

Numerical Model and Baseline Configuration

The flow is modeled using the compressible Navier–Stokes equations for a chemically reacting air mixture in thermal and chemical non-equilibrium. A multi-temperature formulation is adopted to account for vibrational energy relaxation, while species transport and finite-rate chemical kinetics describe dissociation and ionization processes. The gas mixture consists of 11 air species: O_2, N_2, O, N, NO, NO^+, N_2^+ , O_2^+, O^+, N^+, and electrons [12,11]. In this framework, a distinct vibrational temperature is computed for each molecular species, yielding six vibrational temperatures for

Materials Research Proceedings 70 (2026) 20-24 https://doi.org/10.21741/9781644904299-5

ionizing air (O_2, N_2, NO, NO^+, N_2^+, and O_2^+). A separate electronic temperature equation is not included; electronic energy is assumed to be in equilibrium with the translational–rotational mode.

Chemical reactions follow the Park'93 ionizing air kinetic mechanism [12], while transport properties are evaluated using the Gupta–Yos formulation with ambipolar diffusion treatment for charged species [13]. Surface boundary conditions adopt a hybrid catalytic model, assuming non-catalytic behavior for neutral species and full recombination for charged particles [11].

This modeling framework was previously validated in axisymmetric simulations [7] against RAM-C II electron density measurements [4], showing good agreement across the investigated altitude range. Based on this assessment, the same thermochemical configuration is employed for all three-dimensional simulations presented herein.

Geometry, Mesh, and Flight Conditions

The RAM-C II vehicle consists of a hemispherical nose of 0.15 m radius followed by a 9° half-angle cone with a total length of approximately 1.3 m. A high-fidelity three-dimensional CAD model including winglets and base geometry was employed to generate a multi-block structured mesh composed of approximately 1.4 million cells. To ensure asymptotic resolution of the viscous gradients, the mesh is specifically refined in the wall-normal direction. The first-cell height, $\Delta \boldsymbol{y_1}$, was determined based on the local Reynolds number to achieve a non-dimensional wall spacing of $\boldsymbol{y^+ \approx 1}$.

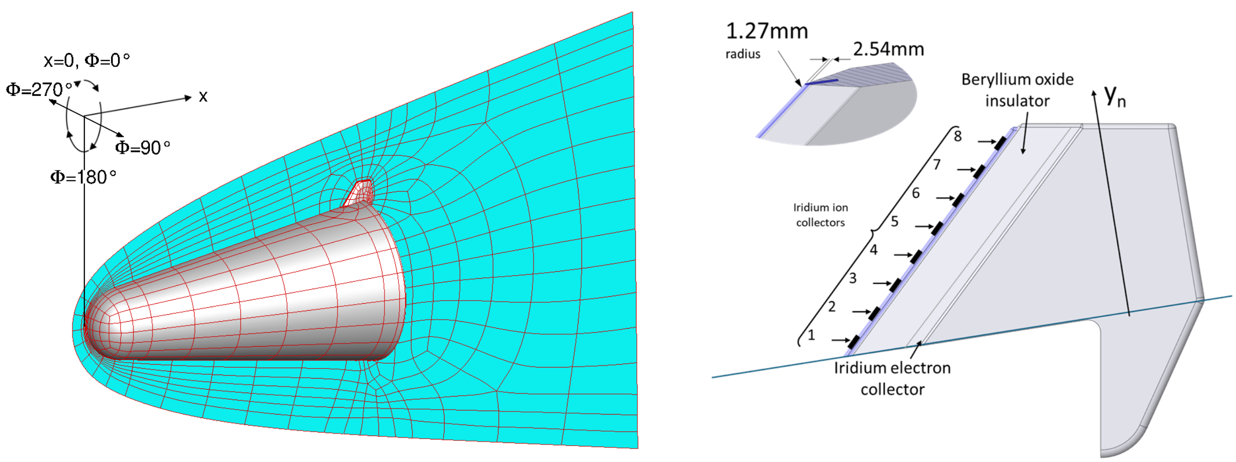

Figure 1: Three-dimensional CAD model of the RAM-C II vehicle used for numerical simulations.

Simulations were performed at altitudes of 61, 71, 76, and 81 km using corresponding freestream conditions from the RAM-C II trajectory. Angles of attack was varied between −4°, −2°, 0°, +2°, and +4°.

Results and discussion

Figure 2 presents peak electron number density distributions along the capsule body for various angles of attack and altitudes.

A clear dependence on vehicle orientation is observed at all altitudes. Negative angles of attack result in significantly increased electron densities relative to the zero-angle case, while positive angles lead to reduced plasma concentrations. The enhancement for negative angles is systematically stronger than the reduction observed for positive angles of equal magnitude. This non-symmetry is most pronounced at lower altitudes, where higher densities and stronger thermo-chemical activity amplify the effects of flow compression and expansion. At higher altitudes, the sensitivity to angle of attack decreases due to reduced reaction rates and increased dominance of diffusive transport.

Materials Research Proceedings 70 (2026) 20-24 https://doi.org/10.21741/9781644904299-5

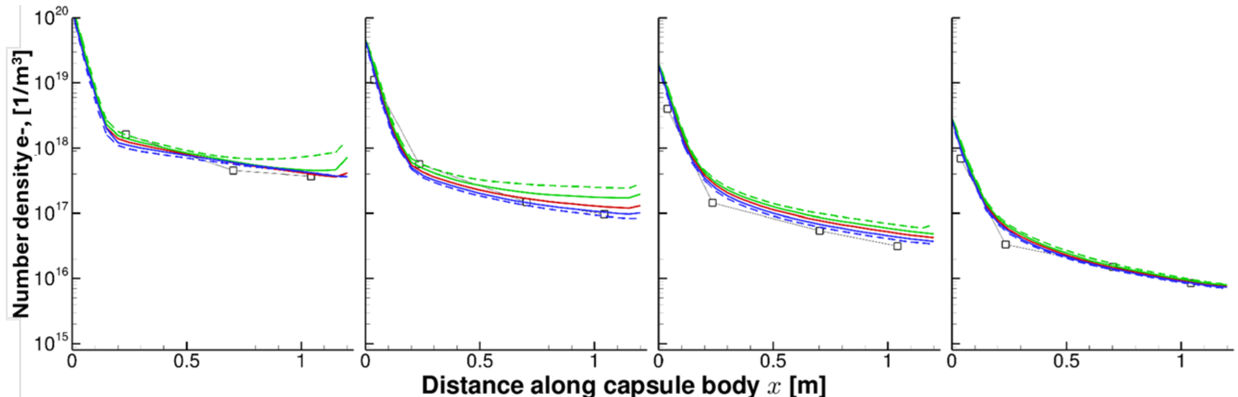

(a) 61km (b) 71km (c) 76km (d) 81km

Figure 2: Electron density profiles along the capsule body at various altitudes for different angles of attack. - - -: AoA=-4°, —: AoA=-2°, —:AoA=0°, —: AoA=+2°, - - -: AoA =+4°.

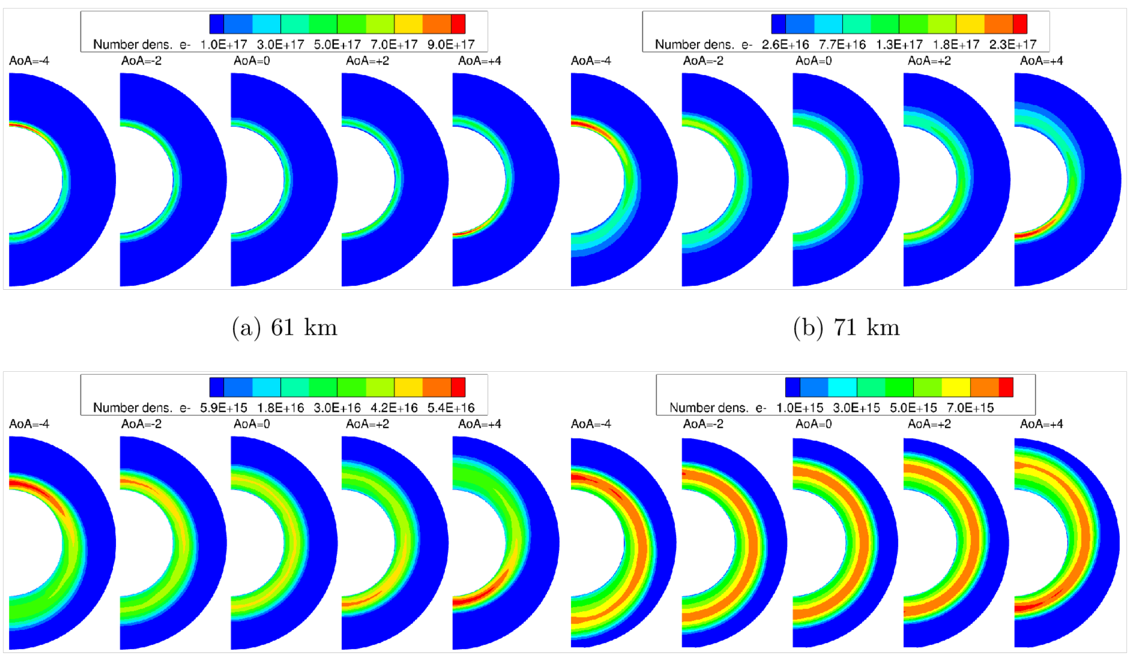

(a) 61 km (b) 71 km

(c) 76 km (d) 81 km

Figure 3: Electron density slices at $x = 1.4$ m for different altitudes and angles of attack.

Cross-sectional slices, extracted at x =1.14 m and shown in Fig. 3, illustrate the spatial asymmetry induced by angle of attack. At lower altitudes, plasma is strongly compressed toward the windward surface for negative angles of attack, while expansion regions exhibit reduced ionization. At higher altitudes the electron density field becomes increasingly uniform and weakly dependent on orientation, indicating that diffusion smooths local gradients.

Electron density profiles extracted along the winglet leading-edge probe line are reported on Fig. 4. Both numerical and experimental data show a noticeable spread attributed to the dynamic motion of the capsule and associated variations in angle of attack during flight. The simulations reproduce this spread and predict an altitude-dependent reduction in sensitivity to orientation.

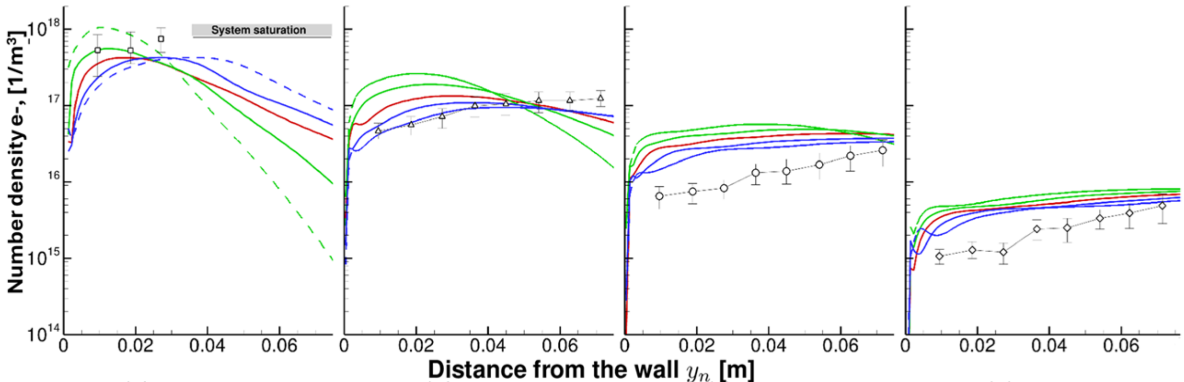

(a) 61km (b) 71km (c) 76km (d) 81km

Figure 4: Electron density profiles along winglet leading edge at various altitudes for different angles of attack. - - -: AoA=-4°, —: AoA=-2°, —:AoA=0°, —: AoA=+2°, - - -: AoA =+4°.

Conclusions

A fully three-dimensional non-equilibrium CFD analysis of the RAM-C II reentry experiment was performed to investigate the influence of angle of attack on plasma formation and electron density distributions.

The validated thermochemical model was extended from axisymmetric to three-dimensional configurations, showing excellent agreement at zero angle of attack. Off-axis simulations revealed strong plasma asymmetries induced by vehicle orientation, particularly at lower altitudes where flow compression and expansion significantly affect ionization processes.

Negative angles of attack produced substantial enhancements in electron density on the windward side, while positive angles led to plasma attenuation on the leeward side. These effects diminished with increasing altitude due to reduced chemical activity and increased diffusive transport.

The three-dimensional simulations successfully reproduced the spread observed in electrostatic probe measurements and captured the altitude-dependent reduction in sensitivity to angle of attack. Overall, the results demonstrate the critical role of three-dimensional flow effects in accurately predicting plasma environments during hypersonic reentry.

References

[1] T.H. Stix, Waves in plasmas, American Institute of Physics, Melville, NY, 1992.

[2] N. Blaunstein, E. Plohotniuc, Ionosphere and applied aspects of radio communication and radar, CRC press, Boca Raton, 2008. https://doi.org/10.1201/9781420055177

[3] S. Esposito, A. Scarabosio, G. Vecchi, D. D'Ambrosio, Non-equilibrium plasma distribution in the wake of a slender blunted-nose cone in hypersonic flight and its effect on the radar cross section, Aerosp. Sci. Technol. 155 (2024) 109699. https://doi.org/10.1016/j.ast.2024.109699.

[4] W.L. Grantham, Flight results of a 25 000-foot-per-second reentry experiment using microwave reflectometers to measure plasma electron density and standoff distance, NASA TR-6662, 1972.

[5] W.L. Jones, A.E. Cross, Electrostatic-Probe Measurements of Plasma Parameters for Two Reentry Flight Experiments at 25,000 Feet per Second, NASA TR-6617, 1972.

[6] G.V. Candler, R.W. MacCormack, Computation of weakly ionized hypersonic flows in thermochemical nonequilibrium, J. Thermophys. Heat Transf. 5 (1991) 266-273. https://doi.org/10.2514/3.260.

[7] L. Cutrone, S. Esposito, A. Schettino, D. D'Ambrosio, Numerical Modeling of Plasma Formation in Hypersonic Flow: A Comparative Study of Thermochemical Models, Proc. 4th Int. Conf. High-Speed Veh. Sci. Technol. (HiSST) (2025) HISST-2025-244.

[8] E. Josyula, W.F. Bailey, Governing Equations for Weakly Ionized Plasma Flowfields of Aerospace Vehicles, J. Spacecr. Rockets 40 (2003) 845-857. https://doi.org/10.2514/2.7036

[9] L.C. Scalabrin, Numerical simulation of weakly ionized hypersonic flow over reentry capsules, Ph.D. Thesis, University of Michigan, 2007.

[10] S. Esposito, D. D'Ambrosio, et al., A Study on Plasma Formation on Hypersonic Vehicles using Computational Fluid Dynamics, Proc. Aerosp. Eur. Conf. 2023 (2023). https://doi.org/10.13009/EUCASS2023-492.

[11] J.G. Kim, S.M. Jo, Modification of chemical-kinetic parameters for 11-air species in re-entry flows, Int. J. Heat Mass Transf. 169 (2021) 120950. https://doi.org/10.1016/j.ijheatmasstransfer.2021.120950.

[12] C. Park, S.H. Lee, Validation of Multi-Temperature Nozzle Flow Code NOZNT, AIAA Paper 1993-2862, 1993. https://doi.org/10.2514/3.622.

[13] R.N. Gupta, J.M. Yos, R.A. Thompson, K-P. Lee, A review of reaction rates and thermodynamic and transport properties for an 11-species air model for chemical and thermal nonequilibrium calculations to 30000 K, NASA RP-1232, 1990.

Numerical Investigation of a High-Enthalpy Flow in an Arc-Jet Facility Using Detailed State-to-State Kinetics

Marco D'AMATO[1,a*], Francesco BONELLI[1,b*], Davide NINNI[1,c], Giuseppe PASCAZIO[1,d], Anselmo CECERE[2,e], Raffaele SAVINO[2,f], Lucia Daniela PIETANZA[3,g], Annarita LARICCHIUTA[3,h], Gianpiero COLONNA[3,i]

[1]DMMM, Politecnico di Bari, Via Re David 200, Bari, Italy

[2]Department of Industrial Engineering, University of Naples Federico II, Naples, Italy

[3]CNR-ISTP, Via G. Amendola 122/D, Bari, Italy

[a]marco.damato@poliba.it, [b]francesco.bonelli@poliba.it, [c]davide.ninni@poliba.it, [d]giuseppe.pascazio@poliba.it, [e]anselmo.cecere@unina.it, [f]rasavino@unina.it, [g]luciadaniela.pietanza@cnr.it, [h]annarita.laricchiuta@cnr.it, [i]gianpiero.colonna@cnr.it

Keywords: Hypersonic Flows, Thermochemical Non-Equilibrium, State-to-State Model

Abstract. This work presents high-enthalpy air flow simulations through a nozzle and the subsequent impingement on a test specimen. An eleven-species air mixture including ions and free electrons is modeled under thermochemical nonequilibrium using a detailed State-to-State (StS) kinetic approach. Results highlight strong deviations from Boltzmann distributions despite moderate roto–translational temperatures. The study provides a consistent assessment of nonequilibrium effects and their impact on the characteristic flow quantities.

Introduction

Thermochemical nonequilibrium at the molecular level can significantly affect the macroscopic behavior of high-enthalpy flows. Nonequilibrium conditions arise when the relaxation times of internal energy modes become comparable to the characteristic flow time, preventing the establishment of local thermodynamic equilibrium. This scenario typically occurs in hypersonic atmospheric entry or high-enthalpy wind tunnels where strong shock waves convert kinetic energy into internal energy, activating vibrational excitation, dissociation, and, at sufficiently high temperatures, ionization processes [1]. Because of these effects, classical equilibrium gas models are inadequate for the description of hypersonic flows. Over the past decades, several approaches have been developed to account for thermal and chemical nonequilibrium. Among them, the multi-temperature (mT) model proposed by Park [2] remains the most widely adopted framework. In this formulation, translational and rotational modes are assumed in equilibrium, while vibrational (and possibly electronic) modes are described by a Boltzmann distribution at a separate temperature. Although computationally efficient and extensively used in engineering applications, the mT approach relies on the assumption of Boltzmann population distributions, which may become inaccurate in the presence of strong gradients, across shock waves, or inside boundary layers [3]. To overcome these limitations, the State-to-State (StS) approach treats individual internal energy levels as independent pseudo-species, directly solving their population evolution without assuming a predefined distribution [4]. This methodology provides a more rigorous description of vibrational kinetics and chemical processes, at the cost of a substantial increase in the size of the chemical system. Thanks to advances in high-performance computing, detailed StS models have progressively become applicable to multidimensional configurations, including nozzle flows [5]. In high-enthalpy experimental facilities, the free-stream conditions impinging on a test article are generated through nozzle expansion. Under such conditions, nonequilibrium effects developing inside the nozzle and, through the subsequent shock forming upstream of the specimen, affect the flow properties and, consequently, the interaction with the test article. In this work, a high-enthalpy air flow through a converging–diverging nozzle is simulated using a detailed State-to-State kinetic model. The exit conditions computed are then employed as free-stream input for the simulation of the flow impinging on an axisymmetric test specimen. The objective of the present study is to characterize the flow structure and thermochemical state inside the nozzle and to assess their impact on the probe surface quantities predicted on the test article, within a fully consistent State-to-State framework.

Mathematical and Numerical Method

Simulations were carried out using an in-house solver [4], which integrates the Navier–Stokes equations for multi-component reacting flows on a multi-GPU platform. An eleven-species air mixture (including ions and free electrons) was considered under thermochemical nonequilibrium conditions, assuming axisymmetric configurations. Since the solver does not support multi-block grids, the two configurations (the flow through the nozzle and the flow impinging on the probe) were treated separately. The nozzle and probe geometries, as well as the nozzle inlet conditions, were taken from an experimental campaign conducted at the University of Naples Federico II [6] within the framework of the HEATS project (PRIN 2022 PNRR). In particular, the flow conditions computed at the nozzle exit section were used as freestream input for the simulation of the flow over the test specimen. As for the probe surface, a fully catalytic wall condition was assumed by adopting the γ-model [7]. The governing equations are discretized using a finite-volume formulation on structured, body-fitted grids. Convective fluxes are evaluated through the Steger and Warming scheme with second-order MUSCL reconstruction, whereas diffusive fluxes are computed by applying the Gauss divergence theorem. A fractional-step (operator-splitting) approach is adopted to decouple fluid-dynamic transport from chemical kinetics. The convective–diffusive terms are advanced in time using an explicit third-order Runge–Kutta scheme, while the stiff chemical source terms are integrated separately by means of an implicit Gauss–Seidel algorithm. Thermochemical nonequilibrium is modeled through a State-to-State (StS) approach [4], which enables a high-fidelity description of non-Boltzmann internal energy distributions. In particular, 68 vibrational levels for N_2 and 47 for O_2 are explicitly considered. Table 1 shows the inlet and the boundary conditions for the nozzle. The inlet mixture composition was determined by imposing thermodynamic equilibrium at the specified total enthalpy and static pressure.

Table 1. Inlet and Boundary Conditions for the Nozzle

Total Enthalpy [MJ/kg]	16.5
Static Pressure [Pa]	21801
Wall Temperature [K]	300
Inlet Mixture Composition	Equilibrium

Results and Discussion

Figure 1 illustrates representative results for the nozzle flow. Specifically, it reports the contour of the vibrational temperature of molecular nitrogen, together with the internal population distribution of N_2 as a function of the energy associated with each vibrational level, evaluated at the point on the symmetry axis corresponding to the nozzle exit section. The flow exiting the nozzle is characterized by a Mach number of 2.98 at the symmetry axis and a rotational–translational temperature of 1906 K. However, as shown in Fig. 1, the flow remains in a strong thermochemical nonequilibrium state. Figure 1 shows that the internal population distribution of nitrogen follows a Boltzmann distribution (the expected equilibrium distribution) only for the lower energy levels, whereas significant deviations from equilibrium are observed for the higher ones. In particular, the intermediate energy levels appear underpopulated, while the highest energy levels are overpopulated. This trend arises from two competing effects: decreasing gas temperature underpopulates intermediate–high energy levels through vibro-translational processes, while recombination dominates at the highest energies, leading to overpopulation.

Starting from the thermodynamic and mixture conditions obtained at the nozzle exit section, simulations of the flow impinging on the probe were performed. The temperature of the catalytic wall was imposed constant and equal to 300 K. The computational grid is structured and consists of 100 × 150 grid points. A mild refinement was introduced in the shock region, while a stronger refinement was applied near the wall, ensuring a first-cell height of 10^{-6} m. Fig. 2 shows the contour plots of roto–translational temperature and free-electron mass fraction.

A strong temperature rise is observed across the bow shock forming upstream of the specimen, with peak values reaching approximately 6000 K. At these temperatures, ionization remains limited; however, a noticeable increase in electron concentration can still be detected. In particular, the highest free-electron mass fraction is found in the post-shock region near the stagnation line, where the local temperature peak enhances ionization processes.

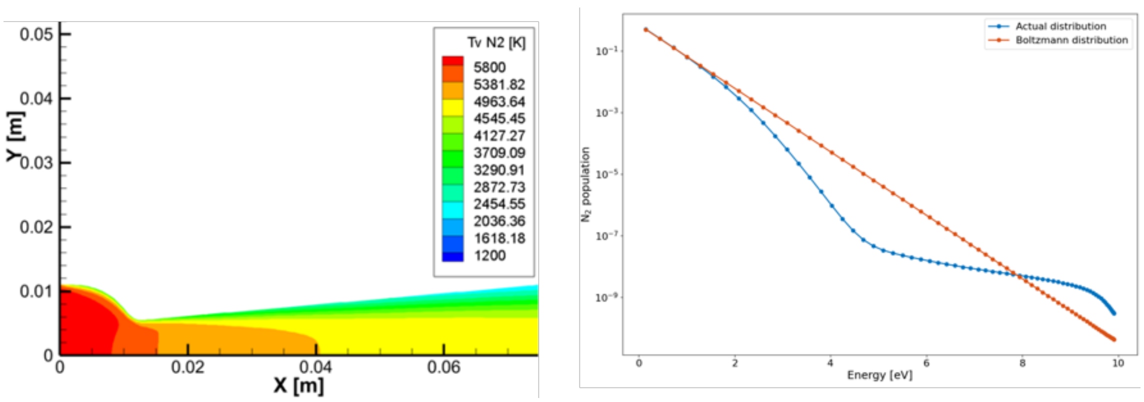

Figure 1. Contour of the vibrational temperature of molecular nitrogen (left); internal population distribution of N_2 as a function of energy, evaluated on the symmetry axis at the nozzle exit (right).

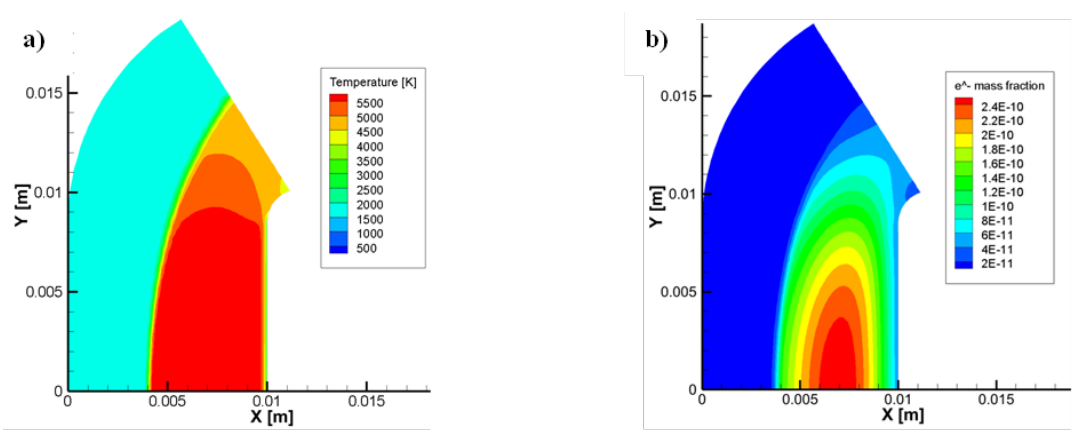

Figure 2. Contours of selected quantities for the fully catalytic wall case using the StS model: a) rotational–translational temperature; b) mass fraction of free electrons. The probe wall is represented by a vertical line with a height of 0.085 m.

Conclusions

In this work, State-to-State simulations of a high-enthalpy air flow through a nozzle and its subsequent impingement on an axisymmetric test specimen have been presented. The results show that the nozzle flow remains in strong thermochemical nonequilibrium up to the exit section, with significant deviations from Boltzmann distributions. These effects directly influence the freestream conditions impinging on the specimen. The study highlights the importance of detailed kinetics for reliable prediction of high-enthalpy flow fields.

Acknowledgements
D.M., B.F., N.D. and P.G. were partially supported by the Italian Ministry of University and Research under the Programme "Department of Excellence" Legge 232/2016 (Grant No. CUP - D93C23000100001).

D.M., B.F., P.G., C.A., S.R., P.L.D., L.A., C.G. were funded by the European Union – Next Generation EU – Piano Nazionale Resistenza e Resilienza (PNRR), Missione 4 Componente C2 Investimento 1.1 – Decreto Direttoriale n. 1409 del 14/09/2022, Bando PRIN 2022 PNRR, CUP Master - D53D23018520001, CUP Politecnico di Bari - D53D23018520001, CUP CNR - B53D23027270001, CUP Università degli Studi di Napoli Federico II - E53D23017480001, Hypersonic Entry flow simulator for Access To Space – HEATS.

The authors acknowledge the CINECA award under the ISCRA initiative, for the availability of high performance computing resources and support under the allocation HP10C6C1WO

References

[1] G. Colonna, F. Bonelli, G. Pascazio, Impact of fundamental molecular kinetics on macroscopic properties of high-enthalpy flows: The case of hypersonic atmospheric entry, Physical Review Fluids 4, 033404 (2019). https://doi.org/10.1103/PhysRevFluids.4.033404

[2] C. Park, Nonequilibrium Hypersonic Aerothermodynamics, Wiley, New York, 1989.

[3] F. Bonelli, D. Ninni, L.D. Pietanza, G. Colonna, B. Helber, T.E. Magin, G. Pascazio, Effects of thermochemical non-equilibrium in the boundary layer of an ablative thermal protection system: A State-to-State approach, Computers & Fluids 270, 106161 (2024). https://doi.org/10.1016/j.compfluid.2023.106161

[4] G. Pascazio, D. Ninni, F. Bonelli, G. Colonna, Hypersonic flows with detailed State-to-State kinetics using a GPU cluster, in: G. Colonna, A. D'Angola (Eds.), Plasma Modeling: Methods and Applications, IOP Publishing, Bristol (2022), pp. 10-1–10-41. https://doi.org/10.1088/978-0-7503-4500-2ch10

[5] F. Bonelli, G. Pascazio, G. Colonna, Effect of finite-rate catalysis on wall heat flux prediction in hypersonic flow, Physical Review Fluids 6, 033201 (2021). https://doi.org/10.1103/PhysRevFluids.6.033201

[6] S. Mungiguerra, G.D. Di Martino, A. Cecere, R. Savino, L. Silvestroni, A. Vinci, L. Zoli, D. Sciti, Arc-jet wind tunnel characterization of ultra-high-temperature ceramic matrix composites, Corrosion Science, 149, 18-28 (2019). https://doi.org/10.1016/j.corsci.2018.12.039

[7] R. Goulard, On catalytic recombination rates in hypersonic flow, Journal of Jet Propulsion 28, 737–745 (1958). https://doi.org/10.2514/8.7444

Materials Research Proceedings 70 (2026) 29-32 https://doi.org/10.21741/9781644904299-7

State-to-State Modeling of the Hypersonic Flow Around the ELECTRE Vehicle

Marco D'AMATO[1,a*], Francesco BONELLI[1,b*], Davide NINNI[1,c], Giuseppe PASCAZIO[1,d], Lucia Daniela PIETANZA[2,e], Annarita LARICCHIUTA[2,f], Gianpiero COLONNA[2,g]

[1]DMMM, Politecnico di Bari, Via Re David 200, Bari, Italy

[2]CNR-ISTP, Via G. Amendola 122/D, Bari, Italy

[a]marco.damato@poliba.it, [b]francesco.bonelli@poliba.it, [c]davide.ninni@poliba.it, [d]giuseppe.pascazio@poliba.it, [e]luciadaniela.pietanza@cnr.it, [f]annarita.laricchiuta@cnr.it, [g]gianpiero.colonna@cnr.it

Keywords: Hypersonic Flows, Thermochemical Non-Equilibrium, State-to-State Model

Abstract. This work investigates hypersonic flow over the ELECTRE re-entry configuration under high-enthalpy conditions. An eleven-species air mixture, including ions and free electrons, is modeled in thermochemical nonequilibrium by means of a detailed State-to-State (StS) kinetic framework. Gas–surface interaction effects are accounted for through a fully catalytic wall model. The simulations provide a detailed characterization of shock structure and internal energy distributions, highlighting the role of non-Boltzmann effects in the stagnation region.

Introduction

High-enthalpy flows occur at temperatures where the calorically perfect gas assumption breaks down. In hypersonic regimes, strong shock waves convert kinetic energy into internal energy, exciting rotational, vibrational and electronic modes and promoting dissociation and ionization. When the relaxation times of these internal processes are comparable to the flow characteristic time, the flow departs from local thermodynamic equilibrium and significant thermochemical non-equilibrium arises. The accurate prediction of such effects is essential for the design of advanced hypersonic re-entry vehicles. Computational tools must therefore solve the Navier–Stokes equations while accounting for complex physico-chemical processes, including vibrational excitation, dissociation, ionization and radiation. Over the years, several finite-rate chemical reaction models have been proposed to describe nonequilibrium effects in hypersonic CFD simulations. Among them, the multi-temperature (mT) framework [1,2] is widely adopted. In this approach, translational and rotational modes are assumed in equilibrium at a common temperature, while vibrational and electronic modes are described by separate temperatures under the assumption of Boltzmann population distributions. However, in strongly nonequilibrium regions such as shock layers, the internal level populations may significantly deviate from Boltzmann equilibrium, thus limiting the predictive capability of such models. To overcome these limitations, the State-to-State (StS) approach [3] provides a more detailed description of thermochemical kinetics. In this formulation, each internal energy level is treated as a pseudo-species and an additional continuity equation is solved for its population. This avoids the assumption of predefined distributions and enables a direct computation of non-Boltzmann internal energy distributions, at the expense of a substantially larger chemical system. In the present work, hypersonic flow over the ELECTRE re-entry configuration [4] is investigated using a detailed State-to-State framework. An eleven-species air mixture, including ions and electrons, is modeled under thermochemical nonequilibrium conditions, and Gas–Surface Interaction (GSI) effects are

Materials Research Proceedings 70 (2026) 29-32 https://doi.org/10.21741/9781644904299-7

taken into account. Simulations are performed with an in-house CFD solver previously validated for neutral mixtures [5], here extended to address ionization-regime applications.

Mathematical and Numerical Method

Numerical simulations were carried out using the in-house CFD solver described in [3], which solves the Navier–Stokes equations for multi-component reacting flows on a multi-GPU architecture. An eleven-species air mixture, including ions and free electrons, was considered under thermochemical nonequilibrium conditions. The ELECTRE vehicle geometry [4] was adopted as reference configuration. Freestream conditions and wall temperature are reported in Table 1. The computational domain extends up to 0.03 m ahead of the stagnation point. A structured, body-fitted grid was generated with 80 cells in the streamwise direction and 120 cells along the vehicle surface. Mesh refinement was applied in the shock region and within the near-wall layer to properly capture steep gradients. In particular, the first cell height at the wall was set to 10^{-6} m. A fully catalytic wall boundary condition was imposed using the γ-model formulation [6]. The governing equations are solved within a finite-volume framework. Inviscid fluxes are evaluated using the Steger and Warming scheme combined with second-order MUSCL reconstruction, while viscous fluxes are computed through the Gauss divergence theorem. Time advancement of the transport terms is performed with an explicit third-order Runge–Kutta method, whereas the stiff chemical source terms are integrated using an implicit Gauss–Seidel procedure [7]. Thermochemical nonequilibrium is modeled through a detailed State-to-State (StS) approach [3]. In this formulation, each vibrational level is treated as a pseudo-species and its population is obtained by solving an additional continuity equation, enabling the direct computation of non-Boltzmann internal energy distributions. Specifically, 68 vibrational levels for $\mathrm{N_2}$ and 47 for $\mathrm{O_2}$ are explicitly included in the kinetic scheme.

Table 1. Freestream conditions and wall temperature for the ELECTRE [4] vehicle

u_∞ $[m/s]$	T_∞ $[K]$	ρ_∞ $[kg/m^3]$	T_w $[K]$
4230	265	6.94×10^{-4}	343

Results and Discussion

Figure 1a) shows the roto–translational temperature distribution around the ELECTRE vehicle under hypersonic freestream conditions ($M_\infty = 13$). A detached bow shock forms upstream of the blunt nose, as expected for high-Mach-number flows over blunt bodies. Across the shock, kinetic energy is rapidly converted into internal energy, leading to a sharp temperature increase within a thin shock layer. Immediately downstream of the shock, the roto–translational temperature reaches a peak value of approximately 8280 K. The intense compression at the stagnation region also results in a stagnation pressure of 11523 Pa, confirming the severe thermodynamic conditions established ahead of the nose. Figure 1b) reports the temperature profile along the stagnation line and its comparison with the numerical results available in [4]. The present solution reproduces the shock location and peak temperature with good agreement. Differences are observed in the shock thickness and in the post-shock relaxation region, which may be attributed to differences in the thermochemical nonequilibrium modeling and numerical resolution adopted in the two studies.

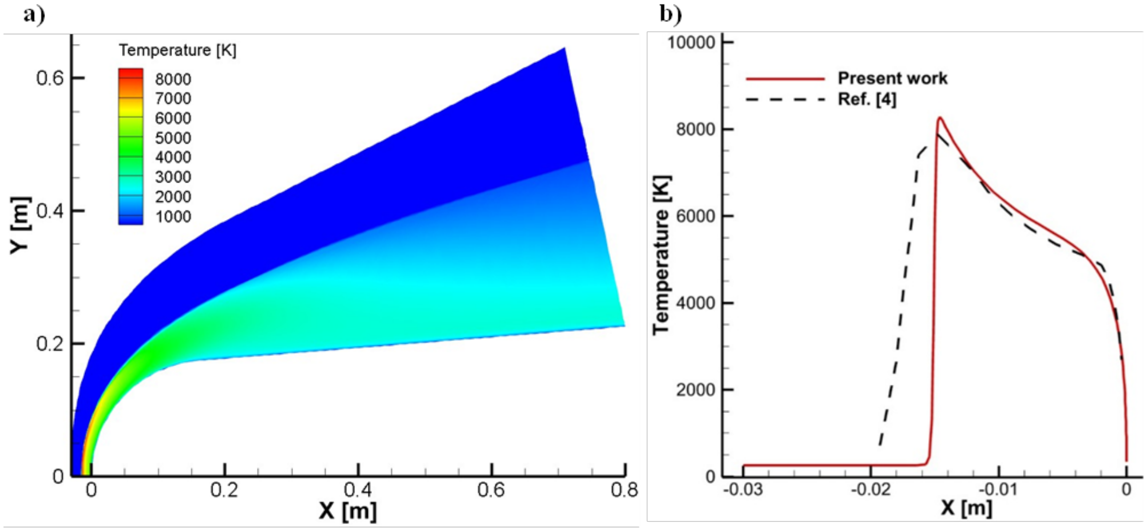

Figure 1. Roto–translational temperature field for the ELECTRE configuration at $M_\infty = 13$: a) contour plot around the entire vehicle; (b) temperature profile along the stagnation line compared with the numerical results reported in [4].

Figure 2 shows the vibrational population distributions of N_2 and O_2 immediately downstream of the bow shock ($x = -0.01$ m), where strong nonequilibrium effects are expected. For N_2 (Fig. 2a), only the lowest-energy levels follow the Boltzmann distribution, whereas the higher-energy states are clearly overpopulated, indicating incomplete vibrational relaxation. For O_2 (Fig. 2b), low and intermediate levels are close to equilibrium, while the highest-energy states are underpopulated. Since these states lie close to the dissociation threshold, molecules populating them are more likely to dissociate than to relax collisionally, leading to their underpopulation. The deviation from the Boltzmann distribution for both species confirms the presence of a strongly nonequilibrium shock layer. The present State-to-State formulation enables the direct resolution of these non-Boltzmann effects, which are particularly relevant in the stagnation region of hypersonic re-entry flows.

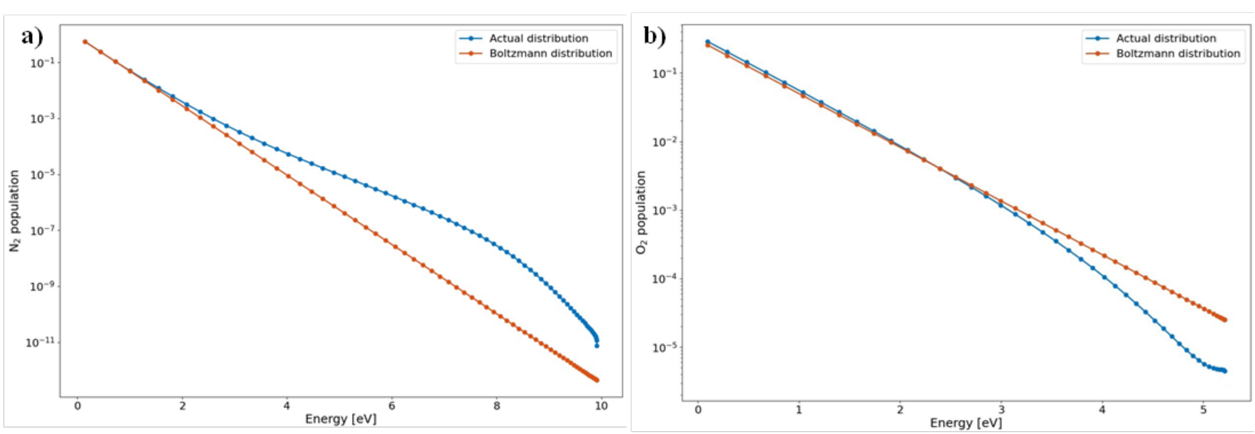

Figure 2. Internal population distribution evaluated at $x = -0.01$ m on the stagnation line as a function of internal energy: a) N_2; b) O_2. Numerical State-to-State results are compared with the corresponding Boltzmann distributions.

Conclusions

Hypersonic flow over the ELECTRE re-entry configuration has been investigated using a detailed State-to-State kinetic model under high-enthalpy conditions. The simulations reproduce the formation of a detached bow shock and the strong thermodynamic gradients in the stagnation region. Results highlight pronounced thermochemical nonequilibrium effects, with internal energy populations significantly departing from Boltzmann distributions immediately downstream of the shock. The analysis confirms that a level-resolved StS framework provides a consistent description of vibrational excitation and relaxation processes in hypersonic re-entry flows, capturing features that simplified equilibrium assumptions would not resolve.

Acknowledgements

D.M., B.F., N.D. and P.G. were partially supported by the Italian Ministry of University and Research under the Programme "Department of Excellence" Legge 232/2016 (Grant No. CUP - D93C23000100001).

D.M., B.F., P.G., P.L.D., L.A., C.G. were funded by the European Union – Next Generation EU – Piano Nazionale Resistenza e Resilienza (PNRR), Missione 4 Componente C2 Investimento 1.1 – Decreto Direttoriale n. 1409 del 14/09/2022, Bando PRIN 2022 PNRR, CUP Master - D53D23018520001, CUP Politecnico di Bari - D53D23018520001, CUP CNR - B53D23027270001, Hypersonic Entry flow simulator for Access To Space – HEATS.

The authors acknowledge the CINECA award under the ISCRA initiative, for the availability of high performance computing resources and support under the allocation HP10B5T7NI

References

[1] C. Park, Nonequilibrium Hypersonic Aerothermodynamics, Wiley, New York, 1989.

[2] R.N. Gupta, J.M. Yos, R.A. Thompson, K.P. Lee, A review of reaction rates and thermodynamic and transport properties for an 11-species air model for chemical and thermal nonequilibrium calculations to 30,000 K, NASA Reference Publication 1232, 1990.

[3] G. Pascazio, D. Ninni, F. Bonelli, G. Colonna, Hypersonic flows with detailed State-to-State kinetics using a GPU cluster, in: G. Colonna, A. D'Angola (Eds.), Plasma Modeling: Methods and Applications, IOP Publishing, Bristol (2022), pp. 10-1–10-41. https://doi.org/10.1088/978-0-7503-4500-2ch10

[4] J. Muylaert, L. Walpot, J. Häuser, P. Sagnier, D. Devezeaux, O. Papirnyk, D. Lourme, Standard model testing in the European high enthalpy facility F4 and extrapolation to flight, AIAA Paper 1992-3905, 1992.

[5] D. Ninni, F. Bonelli, G. Colonna, G. Pascazio, Unsteady behavior and thermochemical nonequilibrium effects in hypersonic double-wedge flows, Acta Astronautica, 191 (2022) 178–192. https://doi.org/10.1016/j.actaastro.2021.10.040

[6] R. Goulard, On catalytic recombination rates in hypersonic flow, Journal of Jet Propulsion 28, 737–745 (1958). https://doi.org/10.2514/8.7444

[7] J.G. Verwer, Gauss–Seidel iteration for stiff ODEs from chemical kinetics, SIAM Journal on Scientific Computing 15, 1243–1250 (1994). https://doi.org/10.1137/0915076

A Computational Study of Positive Corona Discharges for Atmospheric Ionic Propulsion

Giorgio MONGARETTO[1,a], Fabio RAGAZZI[1,b], Arturo POPOLI[1,c *] and Andrea CRISTOFOLINI[1,d]

[1]Department of Electrical, Electronic and Information Engineering "Guglielmo Marconi", University of Bologna, Bologna, Italy

[a]giorgio.mongaretto2@unibo.it, [b]fabio.ragazzi4@unibo.it, [c]arturo.popoli@unibo.it, [d]andrea.cristofolini@unibo.it

Keywords: Electrohydrodynamic Propulsion, Corona Discharge, Ionic Wind, Concentric Wire-Cylinder Corona, Gridded Thrusters, Plasma Fluid Modelling, Atmospheric Pressure Plasmas

Abstract. Plasma-based propulsion is well established for space applications, and recent efforts have focused on extending these concepts to atmospheric operation. Electrohydrodynamic (EHD) thrusters based on corona discharges generate thrust through ion–neutral momentum exchange collisions, producing ionic wind. This work presents simulation results from a one-dimensional drift–diffusion model applied to a concentric wire–cylinder geometry. The same numerical framework is subsequently extended to two dimensions to investigate more complex thruster configurations, such as gridded geometries.

Introduction

In recent years, electrohydrodynamic (EHD) thrusters, originally developed for aerospace applications [1], have attracted increasing interest for atmospheric propulsion owing to their simple design, absence of moving parts, and low acoustic emissions [2]. These devices generate thrust through momentum transfer collisions between ions produced by a corona discharge and neutral molecules (ionic wind principle). A detailed characterization of corona discharges is therefore essential to understand and improve EHD thruster performance and to guide propulsion optimization. In this work, we present numerical results obtained from a one-dimensional, time-dependent drift–diffusion model applied to a concentric wire–cylinder geometry operating with atmospheric pressure air. The simulation results are compared with experimental measurements [3] to validate the model. Subsequently, the numerical framework is extended to a 2D gridded configuration relevant to ionic propulsion. We show the model's ability to predict the onset of back-discharge phenomena caused by intense ionization triggered by high electric fields at the gridded collector edges. This process significantly alters the electrohydrodynamic force density distribution, partially counteracting the ion-driven acceleration of neutral species and ultimately limiting the achievable thrust.

Physical and numerical model

The corona discharge model consists of the continuity equations for each species s, coupled with the electrostatic Poisson's equation, with the flux density expressed under the drift–diffusion approximation:

$$\frac{\partial n_s}{\partial t} + \nabla \cdot \left(-D_s \nabla n_s - \frac{|q_s|}{q_s} \mu_s n_s \nabla \varphi \right) = \Omega_s, \tag{1}$$

Materials Research Proceedings 70 (2026) 33-38 https://doi.org/10.21741/9781644904299-8

Here n_s is the number density of the species s, D_s and μ_s its diffusivity and mobility, q_s its charge value, φ the electric scalar potential and Ω_s the source term that accounts for plasma kinetics. The latter is computed considering a 6-species 13-reaction model of dry air from [4], which considers e, N_2, O_2, N_2^+,O_2^+ and O_2^-. Detailed information on the kinetic model is provided in the appendix. The photoionization process is modelled according to the well-known three-exponential Helmholtz formulation [5]. The temperature of neutrals and ions is assumed to be constant, uniform and equal to the ambient temperature $T = 300$ K. Conversely, electrons are treated using the local field approximation (LFA) [6], where transport and reaction coefficients are assumed to depend solely on the reduced electric field E/N. The electron energy distribution function is obtained using the Boltzmann solver LoKI-B [7], [8]. Dirichlet boundary conditions are imposed for the electrostatic problem: $\varphi = V$ at the powered electrode and $\varphi = 0$ at the grounded electrode. Instead, for the drift-diffusion problem, boundary conditions are taken from [9] and summarized in Table 1.

Table 1: Boundary conditions for particle fluxes, derived from [9]

Species	Positive electrode	Negative electrode
e	$\mathbf{\Gamma} \cdot \hat{n} = n(v_{th}/2 + \mathbf{U}) - 2\mathbf{\Gamma}^+\gamma$	$\mathbf{\Gamma} \cdot \hat{n} = n(v_{th}/2 + \mathbf{U}) - 2\mathbf{\Gamma}^+\gamma$
ion$^+$	$\mathbf{\Gamma} \cdot \hat{n} = n(v_{th}/2)$	$\mathbf{\Gamma} \cdot \hat{n} = n(v_{th}/2 + \mathbf{U})$
ion$^-$	$\mathbf{\Gamma} \cdot \hat{n} = n(v_{th}/2 + \mathbf{U})$	$\mathbf{\Gamma} \cdot \hat{n} = n(v_{th}/2)$

Here $\mathbf{\Gamma}^+$ represents the sum of all positive ion fluxes, $\gamma = 0.01$ is the secondary emission coefficient, $v_{th} = \sqrt{8k_bT/\pi m}$ is the thermal velocity and $\mathbf{U} = sign(q_s)\mu_s\mathbf{E}$ is the drift velocity. Neutrals flux is imposed equal to zero. For the 1D model since the reference electrodes geometry is concentric, the computational domain is represented by a line and it is discretized using a hyperbolic-tangent function, while unstructured triangular meshes, generated by the software GMSH are used for the 2D modelling. The governing equations are discretized using a cell-centered finite volume method (FVM) as in [10]. In Eq. (1), the diffusive and drift terms are discretized respectively with a second-order central difference scheme and a first-order upwind scheme. Both computational models are developed in MATLAB. The time integration is performed using the variable-step, variable-order `ode15s` routine from MATLAB, applied to a differential–algebraic equation (DAE) formulation of the problem. The use of an implicit scheme is essential due to the strong coupling between the species number density and the electric field, and the non-uniformity of the computational grid. In the one-dimensional case (400 nodes), the ratio between the largest and smallest cell sizes is on the order of 400, whereas in the two-dimensional case (40012 cells) the mesh exhibits an extreme scale separation, with a maximum-to-minimum element size ratio of ~10^4. Under these conditions, explicit or semi-implicit schemes constrained by the Courant–Friedrichs–Lewy (CFL) condition would require prohibitively small time steps, especially in the ionization region where drift velocities are high. The resulting system is stiff and nonlinear, and is solved implicitly at each time step. Within the DAE framework, the Jacobian matrix remains sparse, enabling efficient linear solves and favorable scaling with respect to the number of grid elements. Further details of the numerical implementation will be provided in future work.

Simulation results

To validate the numerical model, simulations were compared with experiments reported in [3]. The current-voltage (I-V) curve predicted by the model, shown in Fig. 1, matches experimental data well across a wide voltage range, particularly near the discharge inception. Fig. 2 presents the steady-state spatial distribution of charged species for an applied voltage $V = 40$ kV. As expected, the drift region is dominated by positive ions, indicating that the current is primarily carried by

Materials Research Proceedings 70 (2026) 33-38 https://doi.org/10.21741/9781644904299-8

positive species. Extending the computational framework to two dimensions, a gridded geometry composed of 4 emitter-gridded collector units (each unit is composed of 1 cylindrical emitter and 7 collectors), where each conductor has a radius of $r = 50$ µm, was studied. Periodic boundary conditions were applied at the bottom of the computational domain to investigate the electrical behavior of a 4-unit thruster. For $V = 20$ kV, the high electric field at the grid edge triggers strong ionization, leading to a secondary discharge with negative polarity. This phenomenon, illustrated in Fig. 3 by the large electron population, is known as back-discharge. Electrons subsequently form a broad distribution of negative ions via attachment and recombination processes, creating a negative space-charge-dominated region, as depicted in Fig. 4. The resulting negative space charge modifies the electrohydrodynamic force field (Fig. 5), counteracting part of the ion-induced acceleration of neutrals and thus reducing the attainable thrust.

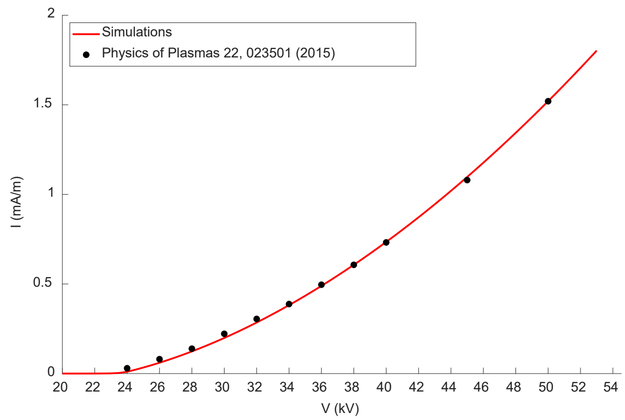

Figure 1: Simulated current–voltage (I–V) characteristic, compared with experimental data [3] for a concentric wire-cylinder geometry with emitter radius r = 700 µm and outer cylinder radius R = 10.35 cm.

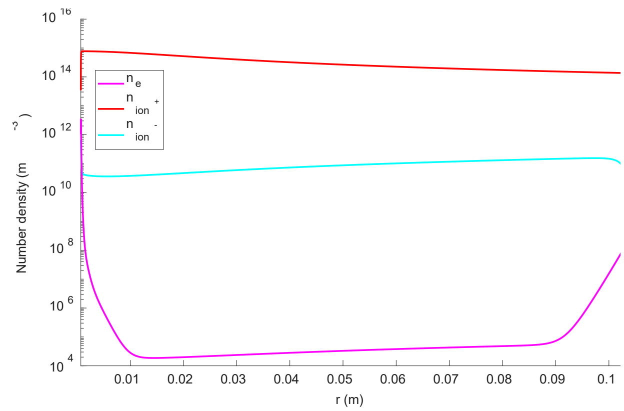

Figure 2: Simulated steady-state number density of charged species ($n^+_{ion} = n_{O_2^+} + n_{N_2^+}$, $n^-_{ion} = n_{O_2^-}$) for a concentric wire-cylinder geometry with emitter radius r = 700 µm and outer cylinder radius R = 10.35 cm.

Conclusions

In this work, positive corona discharge simulations in both one- and two-dimensional configurations are presented. The computed I-V characteristic for a concentric wire–cylinder corona model was validated via a comparison with experimental results. Subsequently, a complex gridded thruster configuration was investigated numerically. An electrical issue associated with the gridded geometry was identified, namely the onset of back-discharge phenomena. This effect alters the space-charge polarity at the grid edge, reducing the total electrohydrodynamic force generated by the thruster and limiting its performance. Future work will focus on the exploration of alternative gridded geometries, including variations in collector number and shape, with the aim of maximizing thrust output. In addition, negative corona modeling will be developed in both one- and two-dimensional configurations to enable the design of a compact system composed of multiple thruster units powered by alternating positive and negative coronas. Such an arrangement is expected to mitigate electrical interference between adjacent units, thereby improving scalability and overall propulsion efficiency.

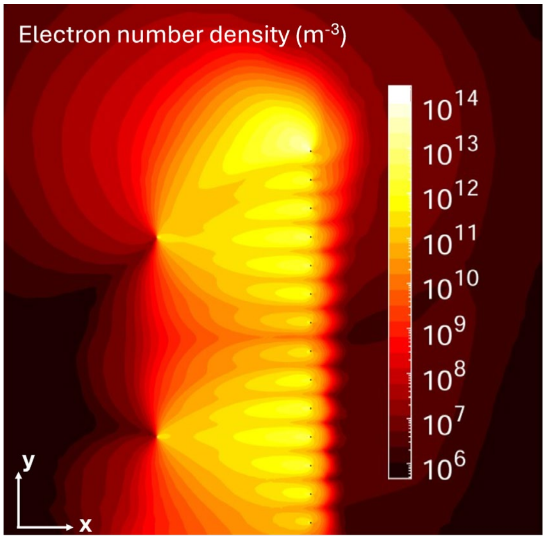

Figure 3: Simulated electron spatial distribution at $V = 20$ kV for a thruster consisting of 4 units, each containing 1 emitter and 7 collectors (symmetry axis on the bottom).

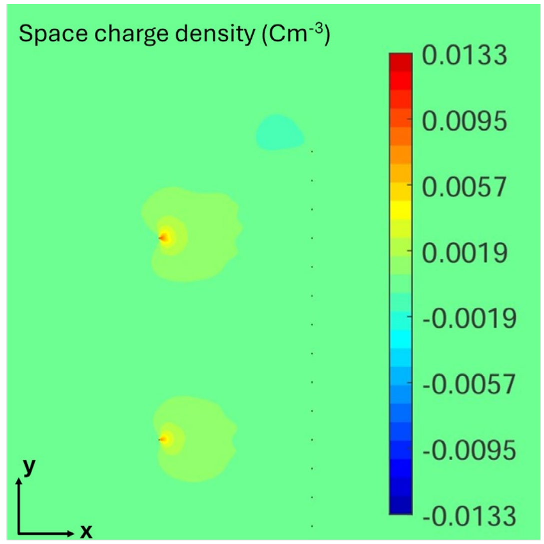

Figure 4: Simulated space charge density at $V = 20$ kV for a thruster consisting of 4 units, each containing 1 emitter and 7 collectors (symmetry axis on the bottom).

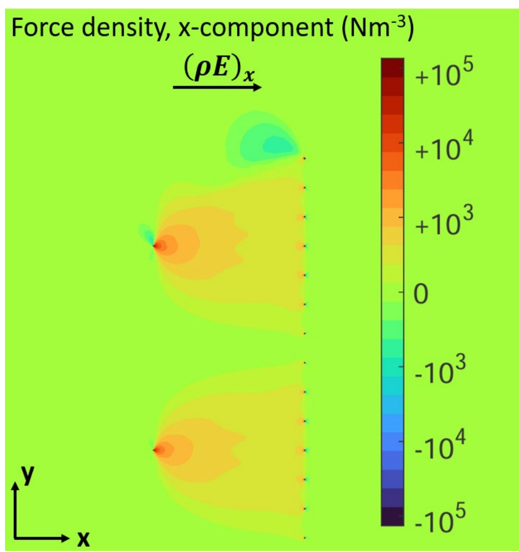

Figure 5: Simulated force density (x-component) at $V = 20$ kV for a thruster consisting of 4 units (symmetry axis on the bottom).

Acknowledgements

Funded by European Union

Funded by the European Union Grant Agreement No 101098900. Views and opinions expressed are however those of the author(s) only and do not necessarily reflect those of the European Union or EISMEA. Neither the European Union nor the granting authority can be held responsible for them.

References

[1] A. Popoli *et al.*, «Hybrid Modeling of Miniaturized 50 W Annular Hall Thruster», *J. Propuls. Power*, vol. 41, fasc. 1, pp. 40–52, gen. 2025. https://doi.org/10.2514/1.B39268

[2] C. E. D. Riboldi *et al.*, «Preliminary Sizing of High-Altitude Airships Featuring Atmospheric Ionic Thrusters: An Initial Feasibility Assessment», *Aerospace*, vol. 11, fasc. 7, p. 590, 2024. https://doi.org/10.3390/aerospace11070590

[3] Y. Zheng, B. Zhang, e J. He, «Current-voltage characteristics of dc corona discharges in air between coaxial cylinders», *Phys. Plasmas*, vol. 22, fasc. 2, p. 023501, feb. 2015. https://doi.org/10.1063/1.4907234

[4] B. Parent, S. O. Macheret, e M. N. Shneider, «Electron and ion transport equations in computational weakly-ionized plasmadynamics», *J. Comput. Phys.*, vol. 259, pp. 51–69, feb. 2014. https://doi.org/10.1016/j.jcp.2013.11.029

[5] A. Bourdon, V. P. Pasko, N. Y. Liu, S. Célestin, P. Ségur, e E. Marode, «Efficient models for photoionization produced by non-thermal gas discharges in air based on radiative transfer and the Helmholtz equations», *Plasma Sources Sci. Technol.*, vol. 16, fasc. 3, p. 656, ago. 2007. https://doi.org/10.1088/0963-0252/16/3/026

[6] L. L. Alves, A. Bogaerts, V. Guerra, e M. M. Turner, «Foundations of modelling of nonequilibrium low-temperature plasmas», *Plasma Sources Sci. Technol.*, vol. 27, fasc. 2, p. 023002, feb. 2018. https://doi.org/10.1088/1361-6595/aaa86d

[7] A. Tejero-del-Caz *et al.*, «The LisbOn KInetics Boltzmann solver», *Plasma Sources Sci. Technol.*, vol. 28, fasc. 4, p. 043001, apr. 2019. https://doi.org/10.1088/1361-6595/ab0537

[8] A. Tejero-del-Caz, V. Guerra, N. Pinhão, C. D. Pintassilgo, e L. L. Alves, «On the quasi-stationary approach to solve the electron Boltzmann equation in pulsed plasmas», *Plasma Sources Sci. Technol.*, vol. 30, fasc. 6, p. 065008, giu. 2021. https://doi.org/10.1088/1361-6595/abf858

[9] V. V. Gorin, A. A. Kudryavtsev, J. Yao, C. Yuan, e Z. Zhou, «Boundary conditions for drift-diffusion equations in gas-discharge plasmas», *Phys. Plasmas*, vol. 27, fasc. 1, p. 013505, gen. 2020. https://doi.org/10.1063/1.5120613

[10] F. Ragazzi, A. Popoli, G. Pierotti, e A. Cristofolini, «A quasi-2D approach for simulating corona discharges in air», in *EPS Conf. Plasma Phys., EPS*, European Physical Society (EPS), 2024.

Appendix

In this appendix, the kinetic scheme and the swarm parameters used in the simulations are presented. Table 2 reports the chemical reactions along with the rate coefficients, while Table 3 reports employed reduced mobilities. The diffusivity D_s for the generic species s is computed through Einstein's relation.

Table 2: 6-species, 13-reaction plasma kinetic model for dry air [4]. E is the electric field magnitude (Vm^{-1}), and T_e is the electron temperature, obtained from the lookup tables generated with LoKI-B [7], [8] (LFA). Both T_e and the gas temperature T are expressed in K. Rate coefficients are given in cm^3s^{-1} for two-body reactions and in cm^6s^{-1} for three-body reactions.

No.	Reaction	Rate coefficient	Ref.
R1	$e + N_2 \rightarrow N_2^+ + 2e$	$\exp[-0.0105809 \cdot \ln(E/N)^2 - 2.40411\times10^{-75} \cdot \ln(E/N)^{46}]$	[4]
R2	$e + O_2 \rightarrow O_2^+ + 2e$	$\exp[-0.0102785 \cdot \ln(E/N)^2 - 2.42260\times10^{-75} \cdot \ln(E/N)^{46}]$	[4]
R3	$e + O_2^+ \rightarrow O_2$	$2.0\times10^{-7} (300/T_e)^{0.7}$	[4]
R4	$e + N_2^+ \rightarrow N_2$	$2.8\times10^{-7} (300/T_e)^{0.5}$	[4]
R5	$O_2^- + N_2^+ \rightarrow O_2 + N_2$	$2.0\times10^{-7} (300/T)^{0.5}$	[4]
R6	$O_2^- + O_2^+ \rightarrow 2O_2$	$2.0\times10^{-7} (300/T)^{0.5}$	[4]
R7	$O_2^- + N_2^+ + N_2 \rightarrow O_2 + 2N_2$	$2.0\times10^{-25} (300/T)^{2.5}$	[4]
R8	$O_2^- + O_2^+ + N_2 \rightarrow N_2 + 2O_2$	$2.0\times10^{-25} (300/T)^{2.5}$	[4]
R9	$O_2^- + N_2^+ + O_2 \rightarrow N_2 + 2O_2$	$2.0\times10^{-25} (300/T)^{2.5}$	[4]
R10	$O_2^- + O_2^+ + O_2 \rightarrow N_2 + 2O_2$	$2.0\times10^{-25} (300/T)^{2.5}$	[4]
R11	$e + 2O_2 \rightarrow O_2^- + O_2$	$1.4\times10^{-29} (300/T_e) \cdot \exp(-600/T) \cdot \exp[700(T_e-T)/(T_eT)]$	[4]
R12	$e + O_2 + N_2 \rightarrow O_2^- + N_2$	$1.07\times10^{-31} (300/T_e)^2 \cdot \exp(-70/T) \cdot \exp[1500(T_e-T)/(T_eT)]$	[4]
R13	$O_2^- + O_2 \rightarrow e + 2O_2$	$8.6\times10^{-10} \cdot \exp(-6030/T) \cdot [1 - \exp(-1570/T)]$	[4]

Table 3: Reduced mobilities ($V^{-1} s^{-1} m^{-1}$) for the 6-species, 13-reaction air plasma kinetic model [4]. E is the electric field magnitude ($V m^{-1}$), N is the gas number density (m^{-3}), and T_e is the electron temperature obtained from lookup tables generated with LoKI-B [7], [8] (LFA). Both T_e and the gas temperature T are expressed in K.

Species	Reduced mobility (μN)	Ref.
e	$3.74\times10^{19} \cdot \exp(33.5 \cdot \ln T_e^{-0.5})$	[4]
O_2^+	$\min[1.18\times10^{23} \cdot T^{-0.5}, 3.61\times10^{12} \cdot (E/N)^{-0.5}]$	[4]
N_2^+	$\min[0.75\times10^{23} \cdot T^{-0.5}, 2.03\times10^{12} \cdot (E/N)^{-0.5}]$	[4]
O_2^-	$\min[0.97\times10^{23} \cdot T^{-0.5}, 3.56\times10^{19} \cdot (E/N)^{-0.1}]$	[4]

Materials Research Proceedings 70 (2026) 39-43 https://doi.org/10.21741/9781644904299-9

Radio-Wave Absorption During Capsule Re-Entry in Atmosphere: A Numerical Study

Oreste PEZZI[1,a *], Davide NINNI[2,b], Francesco BONELLI[2,c] and Gianpiero COLONNA[1,d]

[1]Institute for Plasma Science and Technology, National Research Council of Italy, Via G. Amendola 122/D, Bari, 70126, Italy

[2]Dipartimento di Meccanica, Matematica e Management, Politecnico di Bari, Via Re David 200, Bari 70125, Italy

[a]oreste.pezzi@cnr.it, [b]davide.ninni@poliba.it, [c]francesco.bonelli@poliba.it, [d]gianpiero.colonna@cnr.it

Keywords: Radio-Wave Communication, Computational Fluid Dynamics, Hypersonic Flows, Thermo-Chemical Nonequilibrium, Atmospheric Re-Entry

Abstract. Radio communication during atmospheric re-entry of space vehicles is critical for spacecraft operations due to the formation of a high-temperature plasma which can severely attenuate radio signals. Here, we present a numerical model aimed at investigating radio-wave propagation through the inhomogeneous plasma surrounding the re-entry vehicle. The model employs a one-way coupling of (i) fluid simulations which retain the thermo-chemical non-equilibrium plasma surrounding the capsule, and (ii) a Finite-Difference Time-Domain (FDTD) solver to simulate the interaction of radio-frequency waves with such a plasma flow. This study confirms that radio waves are severely attenuated near the capsule nose.

Introduction

Communication blackout, caused by the formation of a high-temperature, hypersonic, and inhomogeneous plasma layer around the vehicle [1, 2], is a critical challenge during atmospheric re-entry. Accurate modeling of radio wave propagation through the plasma sheath is important for predicting signal attenuation and absorption [3]. Such a plasma is generally in thermo-chemical non-equilibrium as it is composed of a mixture of neutral species, ions, and free electrons, whose densities and temperatures vary sharply along the vehicle surface [4]. In this work, we present numerical results obtained from by one-way combining an axisymmetric two-dimensional (2D) fluid simulation [5], employed to simulate the plasma flow surrounding the capsule, and a FDTD solver implemented for simulating wave propagation [2]. Since we expect a large scale separation between plasma characteristic time scales τ_{plasma} and fluid time scales τ_{fluid}, that is $\tau_{\text{plasma}} \ll \tau_{\text{fluid}}$, the combination of the two numerical methods is one-way and the wave propagation does not back-influence the plasma. Moreover, due to the steady-state solution of the flow field, we focus on a time snapshot of the plasma flow to simulate wave propagation. We show the model's ability to investigate signal absorption. Note that this work describes the first attempts performed by our group for building a coupled CFD-electromagnetic numerical model to investigate the well-known and massively-studied re-entry blackout [6, 7, 8, 9, 10].

Numerical model

As illustrated in Fig. 1, the fluid simulation describes the hot and hypersonic flow ($M_\infty = 5.84$) surrounding a re-entry capsule, providing the flow speed, Mach number, density, temperature, and mass fractions of neutral and ionized species. The simulation is performed by means of a Finite-Volume solver developed at Polytechnic University of Bari (see Ref. [5] and references therein).

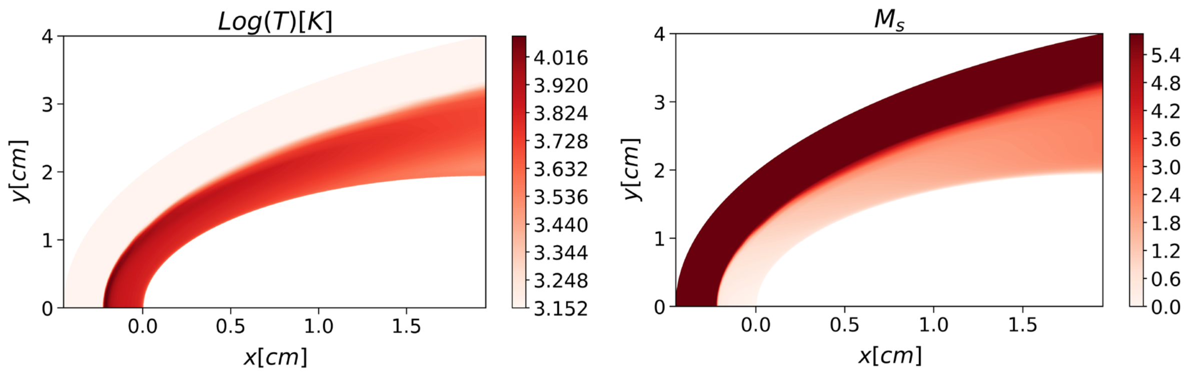

Figure 1: Flow structure around the simulated space capsule. Left and right panels respectively display the flow temperature T and the Mach number M_s.

We considered the Park model [11] with an eleven-species mixture composed of five neutral species (N_2, O_2, NO, N, O), five ions (N_2^+, O_2^+, NO^+, N^+, O^+) and electrons (e^-) to account for charge exchange (e.g., $N^+ + N_2 = N_2^+ + N$) and electron impact processes (e.g., $O + e^- = O^+ + 2e^-$). The free stream mixture is out of chemical equilibrium at a temperature of $T_\infty = T_{v,\infty} = 1428K$, pressure $p_\infty = 1671Pa$, with mass fractions of $Y_{N_2} = 0.62$, $Y_{NO} = 0.0046$, $Y_N = 0.121$, $Y_O = 0.255$, and $Y_{O_2} = 0$. Note that the freestream conditions here adopted are not representative of realistic orbital re-entry due to the significant pre-existing atomic N and O that ensure significant ionization and, hence, strong wave attenuation.

From the local electron density, it is straightforward to compute the electron plasma frequency $f_{p,e} = \omega_{p,e}/(2\pi) \simeq 100 - 1000GHz$, where $\omega_{p,e} = (4\pi n_e\, e^2/m_e)^{1/2}$. We also evaluated the collisional frequency ν_{coll}, being $\nu_{coll} \ll \omega_{p,e}$, as follows. The collisional frequency is computed taking into account both neutrals and ionic species, i.e., $\nu_{coll} = \sum n_\alpha\, \nu_\alpha^{mt}$ where n_α and ν_α^{mt} are the number density and collisional rates of the species α [12]. For both neutrals and charged species, we calculated the collisional frequency rescaling it from the hydrogen one. In particular, for each neutral species, the collisional frequency is computed as:

$$\nu_\alpha^{mt} = \nu_{H(H_2)}^{mt} \left(\frac{M_{H(H_2)}}{M_\alpha}\right)^{1/2}, \quad (1)$$

where M_α is the molar mass of the α species and $\nu_{H(H_2)}^{mt}$ are the collisional frequencies for atomic and molecular hydrogen, computed as:

$$ln\nu_{H(H_2)}^{mt}(T_e) = \sigma(lnT_e: a_1, c_1, l_1) + \sigma(lnT_e: a_2, c_2, l_2) + b\ . \quad (2)$$

The sigmoid function σ is:

$$\sigma(x: a, c, l) = a\frac{exp\left(\frac{x-c}{l}\right)}{exp\left(\frac{x-c}{l}\right)+exp\left(\frac{-(x-c)}{l}\right)}\ ,$$

and a_1, c_1, l_1, a_2, c_2, l_2, and b are fitting parameters [12]. Similarly, for ions, we obtained the collisional frequency starting from the hydrogen ion one, $\nu_H\ =1.86\cdot 10^{-6}/\sqrt{T_K}cm^3s^{-1}$ (being T_K the temperature expressed in Kelvin), as:

$$\nu_\alpha^{mt} = \nu_{H^+}^{mt} \left(\frac{M_{H^+}}{M_\alpha}\right)^{1/2} \frac{q_\alpha^2}{e^2}, \quad (3)$$

where q_α is the ion charge. Note that the 1/2 scaling in Eqs. (1) and (3) with the molar mass ratio underlies the assumption that the cross section σ is weakly dependent on mass so that $\nu_\alpha^{mt}/n_\alpha \sim \sigma v_{th,\alpha} \sim 1/\sqrt{M_\alpha}$.

Then, we implemented the Drude model for estimating the complex permittivity [13], assuming that the radiation frequency ω is in the radio regime $f = \omega/(2\pi) \simeq 1$GHz:

$$\epsilon_r = \epsilon_0 - \frac{\omega_{p,e}^2}{\omega^2+\nu_{coll}^2} \text{ and } \epsilon_i = \frac{\omega_{p,e}^2 \nu_{coll}}{\omega(\omega^2+\nu_{coll}^2)}, \quad (4)$$

where $\epsilon_0 = 1$ is the vacuum permittivity and we also assumed that the magnetic permeability is the vacuum one $\mu = \mu_0 = 1$. The real part of the permittivity is strongly negative as expected in a dielectric plasma, and $|\epsilon_i| \ll |\epsilon_r|$ (not shown here).

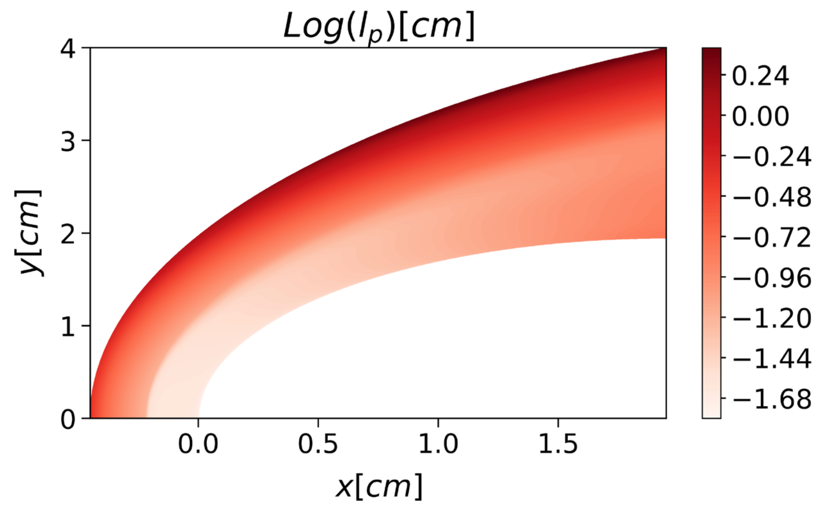

Figure 2: Frequency-dependent electron skin depth $l_p(\omega)$ calculated with f = 2πω = 1GHz.

The frequency-dependent electron skin depth, $l_p(\omega) = \sqrt{c^2/(\omega_{p,e}^2 - \omega^2)}$, quantifies the penetration of radio waves with frequency ω. Since $\omega < \omega_{p,e}$ everywhere, waves are evanescent and the skin depth is smaller than the plasma layer scale, indicating strong absorption. In particular, near the capsule nose $l_p = 10^{-2} cm = 3 \cdot 10^{-2} \lambda$, being the wavelength λ = cf ≃ 30cm.

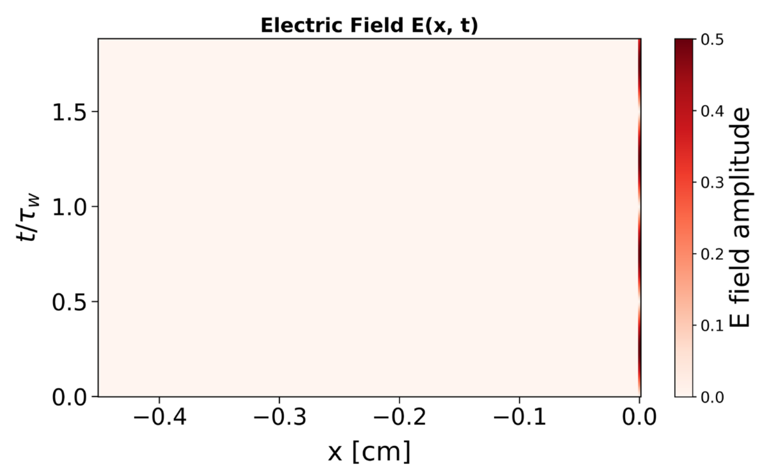

Figure 3: Radiation propagation in the simulation setup obtained through the 1D FDTD algorithm. The radiation is continuously injected from the right domain and is expected to travel backwards.

Finally, plasma permittivity and permeability are used as input for the FDTD algorithm. The FDTD algorithm integrates Maxwell's curl equations adopting finite-difference methods to discretize spatial and temporal derivatives on a staggered Yee-grid [1]. We focus on 1D integrations performed along the horizontal line at y = 0, that is, along the direction transverse to the capsule nose. We first interpolate on a homogeneous one-dimensional grid the relevant quantities, that is, ϵ_r and ϵ_i. The imaginary permittivity is included in the model assuming an effective conductivity $\sigma = \omega\epsilon_i$ [2]. We assume absorbing boundary conditions at $x = x_{min} = -L = -0.45$ cm while a continuous electromagnetic source of radiation of frequency ω is located at $x = x_{max} = 0$ cm. Here, $\Delta x = L/N_x$ with $N_x = 5000$, $\Delta t = \Delta x/c$ and $t_{max} \simeq 1.5\tau_w$ with $\tau_w = 2\pi/\omega$ the wave period. Figure 3 confirms that radiation does not propagate in the plasma layer and is confined to the injection region, confirming the prediction based on the skin depth.

Summary

We developed a numerical framework to quantify radio-wave attenuation around re-entry capsules. Fluid simulations provide plasma parameters, and the Drude model with FDTD integration predicts wave propagation. The study highlights absorption near the capsule nose, emphasizing the impact of plasma formation on communication during atmospheric re-entry. Further developments of this method will include the possibility of mitigating the radio-wave communication blackout by injecting neutral gas [14] and by applying an external magnetic field [15] in the plasma layer surrounding the vehicle. Moreover, considering that the plasma layer can be highly non-uniform in shape and thickness, we plan to investigate the off-axis angular dependence of the transmission in a future study.

Acknowledgements

F.B. was partially supported by the Italian Ministry of University and Research under the Programme "Department of Excellence" Legge 232/2016 (Grant No. CUP - D93C23000100001).

O.P., F.B., G.C. were funded by the European Union – Next Generation EU – Piano Nazionale Resistenza e Resilienza (PNRR), Missione 4 Componente C2 Investimento 1.1 – Decreto Direttoriale n. 1409 del 14/09/2022, Bando PRIN 2022 PNRR, CUP Master - D53D23018520001, CUP Politecnico di Bari - D53D23018520001, CUP CNR - B53D23027270001, Hypersonic Entry flow simulator for Access To Space – HEATS.

References

[1] U.S. Inan and R.A. Marshall. Numerical Electromagnetics: The FDTD Method. Cambridge University Press, 2011. https://doi.org/10.1017/CBO9780511921353

[2] A. Taflove and S.C. Hagness. Computational Electrodynamics: The Finite-Difference Time-Domain Method. Artech House, Norwood, MA, USA, 2005. https://doi.org/10.1002/0471654507.eme123

[3] M.A. Lieberman and A.J. Lichtenberg. Principles of Plasma Discharges and Materials Processing. Wiley-Interscience, Hoboken, NJ, USA, 2005. https://doi.org/10.1002/0471724254

[4] R.B. Bird. Molecular Gas Dynamics and the Direct Simulation of Gas Flows. Oxford University Press, Oxford, UK, 1994. https://doi.org/10.1093/oso/9780198561958.001.0001

[5] G. Pascazio, D. Ninni, F. Bonelli, and G. Colonna. Hypersonic flows with detailed state-to-state kinetics using a GPU cluster. In Plasma Modeling (Second Edition): Methods and applications. IOP Publishing, 2022.

[6] Y. Takahashi, K. Yamada, and T.i Abe. Examination of radio frequency blackout for an inflatable vehicle during atmospheric reentry. Journal of Spacecraft and Rockets, 51(2):430-441, 2014. https://doi.org/10.2514/1.A32539

[7] M. Jung, H. Kihara, K. Abe, and Y. Takahashi. Reentry black-out prediction for atmospheric reentry demonstrator mission considering uncertainty in chemical reaction rate model. Physics of Plasmas, 25(1):013507, 01 2018. https://doi.org/10.1063/1.5010713

[8] A. Scarabosio, J.L.A. Quijano, J. Tobon, M. Righero, G. Giordanengo, D. D'Ambrosio, L. Walpot, and G. Vecchi. Radiation and scattering of em waves in large plasmas around objects in hypersonic flight. IEEE Transactions on Antennas and Propagation, 70(6):4738-4751, 2022. https://doi.org/10.1109/TAP.2022.3142310

[9] S. Esposito, A. Scarabosio, G. Vecchi, and D. D'Ambrosio. Non-equilibrium plasma distribution in the wake of a slender blunted-nose cone in hypersonic flight and its effect on the radar cross section. Aerospace Science and Technology, 155:109699, 2024. https://doi.org/10.1016/j.ast.2024.109699

[10] Y. Takahashi, R. Nakasato, and N. Oshima. Analysis of radio frequency blackout for a blunt-body capsule in atmospheric reentry missions. Aerospace, 3(1), 2016. https://doi.org/10.3390/aerospace3010002

[11] C. Park. Review of chemical-kinetic problems of future NASA missions. I - Earth entries. Journal of Thermophysics and Heat Transfer, 7(3):385-398, 1993. https://doi.org/10.2514/3.431

[12] G. Colonna, A. D'Angola, and A. Laricchiuta. Thermodynamic and transport properties of complex plasmas (chapter 21). In Plasma Modeling (Second Edition) Methods and applications, pages 21-1. IOP Publishing Bristol, UK, 2022. https://doi.org/10.1088/978-0-7503-3559-1ch21

[13] F. F. Chen. Introduction to Plasma Physics and Controlled Fusion, Volume 1: Plasma Physics. Springer, New York, NY, USA, 2016. https://doi.org/10.1007/978-3-319-22309-4_1

[14] T.Miyashita, Y. Sugihara, Y. Takahashi, Y. Nagata, and H. Kihara. Mitigation of reentry blackout via gas injection in arc-heating facility. Journal of Physics D: Applied Physics, 57(32):325206, may 2024. https://doi.org/10.1088/1361-6463/ad4718

[15] D. Felgueiras Luís, A. Viladegut, S.I. Schlachter, M. Dalban-Canassy, J.W. Oswald, G. Herdrich, A. Camps, and O. Chazot. Magnetohydrodynamic effects on radio signal propagation in a plasma flow. Experiments in Fluids, 66(11):211, November 2025. https://doi.org/10.1007/s00348-025-04136-4

Keyword Index

About the Editors

Francesco Bonelli, M.Sc. in Mechanical Engineering and Ph.D. in Industrial and Innovation Engineering, is an Associate Professor at Polytechnic University of Bari. His research focuses on the numerical investigation of high-enthalpy flows involving gas–surface interactions, using advanced thermochemical non-equilibrium models.

Oreste Pezzi, M.Sc. and Ph.D. in Physics, is a Researcher at Consiglio Nazionale delle Ricerche, Institute for Plasma Science and Technology, Bari Branch. His scientific interests include the theoretical and numerical modeling of space and astrophysical plasmas, regarding in particular the fundamental processes, such as plasma turbulence, occurring in these environments.

Anselmo Cecere, M.Sc. and Ph.D. in Aerospace Engineering, is an Associate Professor at University of Naples Federico II. His research activities focus on experimental and numerical fluid mechanics of compressible and incompressible flows for aerospace applications, including Hypersonic Flows, Space Propulsion and MicroGravity.

Davide Ninni, M.Sc. and Ph.D. in Mechanical Engineering, is a Researcher at Polytechnic University of Bari. His research focuses on hypersonic flow modelling and turbulence transition, in the presence of non-equilibrium and gas-surface interactions.

Gianpiero Colonna, M.Sc. in Physics and Ph.D. in Chemistry, is a Research Director at Consiglio Nazionale delle Ricerche, Institute for Plasma Science and Technology, Bari Branch. His scientific interest is focused on the modelling of plasma in different systems and conditions, in both equilibrium and non-equilibrium conditions.